Fluid-mediated, brittle-ductile deformation at seismogenic depth: Part I- Fluid record and deformation history of fault-veins in a nuclear waste repository (Olkiluoto Island, Finland)

Barbara Marchesini[1§], Paolo Stefano Garofalo[1], Luca Menegon[2], Jussi Mattila[3] and Giulio Viola[1]

[1]Dipartimento di Scienze Biologiche, Geologiche e Ambientali, Università di Bologna, Italy
[2]School of Geography, Earth and Environmental Sciences, University of Plymouth, PL48AA Plymouth, UK
[3]Geological Survey of Finland (GTK), Espoo, Finland

[§]*Correspondence to*: barbara.marchesini2@unibo.it

Abstract. The dynamic evolution of fault zones at the seismogenic brittle-ductile transition zone (BDTZ) expresses the delicate interplay between numerous physical and chemical processes. Deformation and fluid flow at the BDTZ are closely related and mutually dependent during repeating and transient cycles of frictional and viscous deformation. Despite numerous studies documenting in detail seismogenic faults exhumed from the BDTZ, uncertainties remain as to the exact role of fluids in facilitating broadly coeval brittle and ductile deformation at that structural level. We combine structural analysis, fluid inclusion and mineral chemistry data from synkinematic and authigenic minerals to reconstruct the temporal variations in fluid pressure (P_f), temperature (T), and bulk composition (X) of the fluids that mediated deformation and steered strain localization along BFZ300, a strike-slip fault originally active at the BDTZ. BFZ300 deforms the Paleoproterozoic migmatitic basement of southwestern Finland and hosts in its core two laterally continuous quartz veins formed by two texturally distinct types of quartz – Qtz I and Qtz II, with Qtz I older than Qtz II. Veins within the damage zone are formed exclusively by Qtz I. Meso- and microstructural analysis combined with fluid compositional data indicate recurrent cycles of mutually overprinting brittle and ductile deformation triggered by oscillations of fluid pressure peaking at 210 MPa. Fluid inclusion microthermometry and mineral pair geothermometry indicate that the two documented quartz types precipitated from different fluid batches, with bulk salinities in the 1-5 wt% NaCleq range for Qtz I and in the 6-11 wt% NaCleq range for Qtz II. The temperature of the fluids involved with initial strain localization and later fault reactivation evolved through time from > 350 °C during Qtz I precipitation to < 300 °C at the time of Qtz II crystallization. The peak fluid pressure estimates constrain pore pressure oscillations between 80 and 210 MPa during the recorded faulting episodes. Our results suggest variability of the physico-chemical conditions of the fluids steering deformation (P_f, T, X) reflecting the ingress and effects of multiple batches of fluid in the fault zone. Initial, fluid-mediated embrittlement generated a diffuse network of joints and/or hybrid/shear fractures in the damage zone; subsequent strain localization led to more localized deformation within the fault core. Localization was guided by cyclically increasing fluid pressure and transient embrittlement of a system that was otherwise under overall ductile conditions.

33   Our analysis suggests that fluid overpressure at the BDTZ can play a key role in the initial embrittelment of the deforming rock
34   and steer subsequent strain localization.

36   **1 Introduction**

37   The physical and chemical properties of fault systems play a fundamental role in controlling the rheological behaviour of the
38   Earth's crust and in steering channelled fluid flow (e.g. Caine et al., 1996). Deformation and fluid flow are closely related and
39   mutually dependent via a number of feedbacks, such as the control that fluids exert upon the effectiveness of deformation
40   processes and the development of fault systems at all scales, and the control by rock heterogeneities and/or fracture system
41   topology on the net fault transmissivity (e.g. Crider and Peacock, 2004). The nucleation and development of permeable fault
42   systems and the mechanisms whereby individual faults may weaken and eventually fail are, therefore, complex functions of a
43   number of processes. In this perspective, the interaction between fluid and mineral phases within fault rocks needs to be studied
44   with a system approach in order to single-out the role and importance of all processes involved (Kaduri et al., 2017).
45   An obvious effect of fluid involvement, particularly in crustal volumes that have experienced large deformation-controlled fluid
46   fluxes, is the precipitation of authigenic and hydrothermal minerals within faults (Oliver and Bons, 2001; Viola et al., 2016) and
47   their immediately adjacent host rock (Mancktelow and Pennacchioni, 2005; Garofalo, 2004). In the seismogenic region of the
48   crust, where fluids may even be the primary driver of the seismic cycle (e.g Miller, 2013), faults have been shown to have the
49   potential to function like a "fluid-activated valve", whereby they experience transient and cyclic fluid pressure build-up before
50   sudden fluid venting, pore pressure- and mechanical strength drop concomitant with seismic failure (e.g. Sibson, 1989, 1992b,
51   1993; Cox, 1995;Viola et al., 2006; De Paola et al., 2007; Wehrens et al., 2016). Hydrothermal ore deposits, where fault networks
52   focus relatively large volumes of ore fluids and precipitate economic minerals (Cox et al. 2001; Boiron et al., 2003; Moritz et al.,
53   2006; Scheffer et al., 2017a) are also pertinent examples of significant deformation-controlled fluid ingress.
54   The seismogenic depth down to 10-15 km (e.g. Kohlstedt et al., 1995) is thus a key region of the crust where to study the whole
55   range of fluid-rock interaction processes occurring within fault zones. Deformation at that depth might be accommodated under
56   overall brittle-ductile conditions along fault systems crossing or rooting into the brittle ductile transition zone (BDTZ). In detail,
57   the deformation style in the BDTZ is generally characterized by the cyclicity, also at the short time scale, between brittle and
58   ductile behaviour (Famin et al., 2004; Famin et al., 2005; Siebenaller et al., 2013). This is induced and regulated by the complex
59   and transient interplay of numerous parameters, among which the lithological composition and transient variation of temperature,
60   pore pressure and strain rate within the deforming system. Field studies have documented unequivocally that ductile and brittle
61   deformation may even be simultaneously active during deformation as a function of the transient and spatially heterogeneous
62   evolution of the chemical and physical parameters steering deformation, leading to the broad coexistence of geological features
63   expressing frictional deformation and viscous creep, and to mutual crosscutting relationships thereof (e.g., Guermani and
64   Pennacchioni, 1998; Kjøll et al., 2015; Pennacchioni et al., 2006; Wehrens et al., 2016; Scheffer et al., 2017b).

65 Veins are particularly important in this context because they attest to the relative abundance of aqueous fluids in the deformation

66 history (e.g. Cox et al., 2001). Portions of the seismogenic crust that experience large fluid fluxes host pervasive and vertically

67 extensive vein networks (Sibson et al., 1988), within which up to several millions of m^3 of hydrothermal minerals may deposit

68 from the flowing fluid (e.g. Heinrich et al., 2000; Cox, 2005; Bons, 2001; Garofalo et al., 2002). In contrast, portions of the crust

69 deforming in the absence of significant fluid flow would show scarce evidence of- or no veining, with only synkinematic H_2O-

70 rich minerals within the fault rock attesting to hydrous conditions (cf. Mancktelow and Pennacchioni, 2004; Menegon et al.,

71 2017).

72 The physical-chemical conditions of fluid-rock interaction in the BDTZ have been studied within exhumed faults by applying a

73 set of geochemical tools that include fluid inclusion analysis (e.g. Morrison, 1994; Morrison and Anderson, 1998; Mulch et al.,

74 2004; Ault and Selverstone, 2008; Garofalo et al., 2014; Siebenaller et al., 2016; Compton et al., 2017), determination of the

75 isotopic compositions of fault fluids, and mass transfer calculations between host rock and fault rocks (e.g. Goddard and Evans,

76 1995; Garofalo, 2004; Mittempergher et al., 2014; Spruzeniece and Piazolo, 2015). This approach yields important constraints

77 on the PT conditions of fluid-rock interaction within the BDTZ, on the source region of the fluids reaching and flowing within

78 the deformation zones, and on element mobility during syn-tectonic fluid flow. These studies, however, do not specifically address

79 the role of fluids on the mechanisms that trigger and permit the aforementioned cycles of brittle-ductile deformation. Open

80 questions thus remain, such as, for example, which pressure, temperature, composition (P, T, X) conditions are best for a fluid to

81 trigger brittle-ductile deformation cycles in a fault system within the BDTZ and which fluid property is specifically most effective

82 in controlling the cycles.

83 In this work, we follow a multidisciplinary approach by combining meso- and microstructural observations with the geochemical

84 analysis of fluids, petrographic documentation of fault rocks and veins, microthermometric properties of fluid inclusion

85 assemblages, electron probe microanalyses (EPMA) of fault minerals, Raman spectrometry of fluid inclusions, and electron probe

86 cathodoluminescence imaging to study the effects of numerous cycles of fluid-rock interaction that have occurred in a vein-rich

87 deformation zone at the seismogenic BDTZ and now exhumed as part of the Paleoproterozoic continental crust of southwestern

88 Finland. The studied deformation zone belongs to an exhumed conjugate fault system that experienced a complex history of

89 structural reactivation and fluid flow. Deformation zone BFZ300, the target of our study, crops out at c. 426 m below sea level

90 within the deep Onkalo nuclear waste repository that is presently being built in the island of Olkiluoto (Fig. 1a).

91 Our results allow us to constrain and describe the progressive evolution of the deformation processes and the role of fluids

92 involved both at fault initiation and during the subsequent reactivation phases. We propose that fluid pressure fluctuation cycles

93 within an overall ductile environment at the BDTZ triggered brittle-ductile cyclicity encompassing fracturing, vein precipitation

94 and crystal-plastic deformation before renewed and fluid-induced embrittlement. Our multitechnique approach made it possible

95 to determine many of the actual chemical and physical properties of the fluids involved in the deformation process, leading to a

96 well-constrained conceptual mechanical model for the fault nucleation and subsequent development.

2 Geological setting

The study area is located in southwestern Finland, on the island of Olkiluoto (Fig. 1a) within the Paleoproterozoic Svecofennian orogenic province, which is formed by supracrustal high-grade metamorphic sequences and plutonic rocks. The most abundant lithologies in the study area are variably migmatitic metasedimentary rocks interleaved with up to several meter thick levels of metavolcanic rocks in addition to calc-alkaline synorogenic TTG-type granitoids, as well as late orogenic leucogranites (Figs. 1a, 1b). For a detailed lithological characterization of the area, we refer the reader to Hudson and Cosgrove (2006) and Aaltonen et al. (2016).

Numerous studies carried out on Olkiluoto have highlighted the long geological evolution of the region, which is commonly summarised by tectonic models proposing either an evolution during a single and semi-continuous Svecofennian orogenic event (Gorbatschev and Bogdanova, 1993) or, alternatively, a sequence of up to five distinct accretion events leading to the amalgamation of several microcontinents and island arcs at the margin of the Archean craton between 1.92 and 1.79 Ga (e.g. Lahtinen et al., 2005). In this scenario, several subduction systems developed, and the collision of the involved microcontinents and island arc complexes resulted in conspicuous continental growth, forming the major part of the Paleoproterozoic domain of the Fennoscandian Shield (1.89-1.87 Ga). According to Lahtinen et al. (2005), this "Fennian accretionary event" ended with a phase of orogenic collapse associated with regional extension and remarkable crustal thinning between c. 1.86 and 1.84 Ga. Renewed compression ensued during collision of the "Sarmatian Plate" with the previously consolidated Svecofennian Shield, causing major crustal shortening, high temperature regional metamorphism (Kukkonen and Lauri, 2009) and the emplacement of S-type granites (e.g. Ehlers et al., 1993). Tectonic activity ascribable to this orogenic phase ceased with a distinct orogenic collapse phase at 1.79-1.77 Ga (Lahtinen et al., 2005).

Pervasive reworking of the Svecofennian domain took place in the Mesoproterozoic when the crust underwent significant stretching and was intruded by voluminous Rapakivi granites and diabase dykes resulting from the widespread melting of the lower crust at c. 1.65-1.50 Ga. This tectonic phase was probably due to the development of a rift along the present Baltic Sea (Korja et al., 2001). Crustal thinning caused also the formation of the "Satakunta Graben", a NW-SE trending graben located c. 50 km to the north of Olkiluoto, which was later filled by Mesoproterozoic sandstone (Jotnian sandstones, Fig. 1a). The latest stage of crustal evolution in southern Finland is expressed by the intrusion of 1.27-1.25 Ga, N-S striking olivine diabase dikes (Fig. 1a; e.g., Suominen, 1991).

As to the structural evolution of the study area, the bedrock was affected by complex, polyphase ductile deformation between 1.86 and 1.81 Ga. According to the evolutionary deformation scheme by Aaltonen et al. (2010) the results of up to five different phases, referred to as D_1-D_5, are preserved in the local structural record, each characterised by structures with distinctive mineral composition, metamorphic grade, geometry and kinematics. The most relevant phases to our study are D_2 to D_4. During these ductile episodes, a regional and pervasive NE-SW striking and moderately SE-dipping foliation developed, strain localized along mesoscopic shear zones parallel to subparallel to the foliation and extensive migmatization occurred under amphibolite-facies metamorphic conditions. NNE-SSW and N-S striking mylonitic shear zones also formed under those conditions, whereas later

130 ductile events developed under progressively lower-grade metamorphism until c. 1.7 Ga ago, when brittle deformation became

131 the dominant deformation style in response to progressive regional exhumation and cooling (Mattila and Viola, 2014; Aaltonen

132 et al., 2016). The penetrative, inherited ductile grain that by then characterised the crystalline basement and that was suitably

133 oriented with regard to the prevailing stress field was invariably reactivated. This is the case for several NNE-SSW striking faults

134 mapped underground in the Onkalo repository, which clearly overprint earlier D4 shear zones and fully exploit the pre-existing

135 ductile precursors. Other faults, such as BFZ300, do not show any clear genetic relation to the older ductile fabric and cut

136 it discordantly.

137 As shown in the following section, BFZ300 belongs to a set of subvertical, conjugate brittle-ductile to fully brittle strike-slip

138 faults characterized by N-S-trending sinistral and NW-SE dextral faults. Both sets document a complex history of reactivation

139 and contain evidence for cyclic and transient switches between brittle and ductile deformation at all scales. Meso- and

140 microstructural studies show that the sinistral faults overprint and probably reactivate a dextral mylonitic precursor related to

141 earlier, localized ductile deformation (Prando et al., in prep.). These faults locally contain pseudotachylyte injections, which

142 suggests seismic behaviour during deformation (Menegon et al., 2018). In contrast, dextral faults cut across the foliation, do not

143 exploit any ductile precursors and do not host pseudotachylytes. BFZ300 belongs to this second group of faults. In the following,

144 we describe its architecture, reconstruct its deformation history and constrain the deformation mechanisms and faulting conditions

145 that prevailed during its nucleation and subsequent development. The architecture and deformation history of the remarkably

146 different conjugate structure to BFZ300, which is a sinistral brittle-ductile deformation zone, is described in the Part II

147 companion paper (Prando et al., in prep.).

3 Methods: Fluid inclusions, mineral chemistry and EBSD analyses

149 Field documentation and sampling were carried out at the underground Onkalo exposures of BFZ300 (Fig. 1b) which were

150 necessarily limited in extent to the actual excavated volume of rock at the time of our study but that, together with the logged

151 diamond drill cores from the underground exploration, allow a well-constrained 3D reconstruction of the local geology.

152 Fluid inclusion measurements were conducted on "fluid inclusion assemblages" – FIAs, i.e. on petrographically discriminated,

153 cogenetic groups of fluid inclusions located along trails or (less commonly) within clusters (Bodnar, 2003a; Goldstein, 2003). By

154 definition, FIAs are groups of inclusions that have been trapped together (i.e., they are cogenetic) at a specific stage of mineral

155 formation and, as such, give the highest level of confidence when characterizing the properties of trapped fluids and discriminating

156 possible stages of post-entrapment re-equilibration (Bodnar, 2003b, and references therein). We applied Roedder's identification

157 criteria of FIAs according to the timing of entrapment (i.e., primary, secondary, pseudosecondary) in order to link stages of fluid

158 entrapment with stages of brittle and ductile deformation of quartz. In this regard, we considered as cogenetic, and therefore

159 representative of one specific stage of brittle deformation and fluid circulation, only those FIAs that exhibited both similar

160 orientation and petrographic characteristics at the scale of the thin section.

In the selected samples, we studied 28 FIAs entrapped within two distinct generations of quartz (named Qtz I and Qtz II) forming two different generations of veins and exhibiting the least petrographic evidence of post-entrapment overprinting by later ductile and/or brittle deformation, which provided c. 800 microthermometric properties. Due to the well-documented tendency of fluid inclusions to modify their shape, volume, and composition after their initial entrapment even at low deviatoric stress conditions (e.g. Diamond et al., 2010; Kerrich, 1976; Tarantola et al., 2010; Wilkins and Barkas, 1978), working on FIAs that show the least possible degree of textural re-equilibration is essential when aiming at constraining the physical and chemical properties of the fluid(s) involved in the fault activity.

Microthermometric properties of fluid inclusions were determined at the Department of Biological, Geological and Environmental Sciences of the University of Bologna using a Linkam THMSG 600 heating/freezing stage coupled with an Olympus BX51 polarizing microscope. The microthermometry stage was calibrated by using synthetic fluid inclusion samples at -56.6, 0.0, and 374 °C, which correspond to the melting of CO_2, ice melting, and final homogenization of H_2O inclusions, respectively. Obtained accuracies were ±0.3 °C for final ice melting temperature (Tm_{ice}) and ±3 °C for final homogenization temperature (Th_{tot}). In order to produce an internally consistent dataset, all phase transitions were exclusively collected for individual FIAs and measured with the same standard procedure. Samples were first rapidly cooled to c. -180 °C and then slowly heated to detect the potential formation of a solid carbonic phase, eutectic phases, salt hydrates, ice, and clathrates. The Th_{tot} were later determined in the FIAs by heating the samples from room temperature and recording the mode of homogenization (i.e., by bubble or liquid disappearance). All phase transitions were measured by using the cycling method described by Goldstein and Reynolds (1994), and care was taken also to record the minimum and maximum values for each assemblage. Volume fractions of individual fluid inclusions determined as % of the ratio $\varphi=V_v/V_{tot}$ (cf. Diamond, 2003), were estimated optically at room temperature using calibrated charts. Salinity, bulk densities and isochores were computed from the measured Tm_{ice} values using the HokieFlincs Excel spreadsheet (Steele-MacInnis et al., 2012 and references therein).

Fluid inclusions were also analysed using micro Raman spectrometry. Analyses were carried out at the Department of Mathematical, Physical and Computer Sciences of the University of Parma (Italy) using a Jobin-Yvon Horiba LabRam spectrometer equipped with He–Ne laser (emission line 632.8 nm) and motorized XY stage. The spectral resolution of the measurements was determined as nearly 2 cm^{-1}. The confocal hole was adjusted to obtain a spatial (lateral and depth) resolution of 1–2 µm. Most spectra were obtained with a 50× objective (N.A. 0.75), although for shallow inclusions also a 100× objective (N.A. 0.90) was used. The calibration was made using the 520.7 cm^{-1} Raman line of silicon. A wide spectral range (100–3600 cm^{-1}) was scanned for each inclusion for the presence of CO_2, N_2, CH_4, and H_2S, but the final acquisitions were made mainly between 1100 and 1800 cm^{-1} for the study of CO_2 spectra, and between 2500 and 3300 cm^{-1} for CH_4 and H_2S. The acquisition time for each spectral window was 120–240 s, with two accumulations. The power on the sample surface is nearly 1 mW but the power on the analysed inclusions has to be considered lower due to reflections and scattering. Analyses were carried out on the vapour bubbles of the fluid inclusions.

193 After the calculation of representative fluid inclusion isochores for each FIA, the pressure corrections were assessed by using the

194 crystallization temperatures of two mineral pairs – namely chlorite-quartz and stannite-sphalerite – as independent input

195 parameters. Chlorite-quartz temperatures were calculated by using the method of Bourdelle and Cathelineau (2015), which

196 assumes quartz-chlorite equilibrium and uses ratios of chlorite end-member activities to link the chlorite compositions with the

197 corresponding formation temperatures through the quartz-chlorite equilibrium constants. This method is based on

198 measurements of the concentrations of the major chlorite components (Si, Fe, Mg) and can only be applied to chlorites with (K_2O

199 $+ Na_2O + CaO$) < 1wt%, indeed the case of our chlorites. To estimate the formation temperature of cogenetic sulphides associated

200 with Qtz II we used the stannite-sphalerite formation temperature following the method proposed by Shimizu. and Shikazono

201 (1985). This geothermometer uses the temperature dependency of iron and zinc partitioning between stannite and sphalerite

202 (Nekrasov et al., 1979) as a temperature indicator of the association Qtz II-stannite and sphalerite.

203 Electron Probe Microanalysis (EPMA) of fault minerals was carried out with a JEOL-8200 wavelength-dispersive electron

204 microprobe housed at the Department of Earth Sciences of the University of Milan, Italy. The instrument fits 5 WDS

205 spectrometers utilizing lithium fluoride (LiFH), pentaerythritol (PETJ and PETH), and thallium acid pthalate (TAP) analysing

206 crystals and an optical microscope. Samples were probed with a beam size of ~1 μm at 15 keV and 5 nA beam current. Synthetic

207 and natural materials were used as calibration standards at the beginning of each session. Analytical 1-σ errors are typically < 4%

208 for major elements and for the minor elements.

209 Panchromatic cathodoluminescence (CL) imaging was also performed by using the CL CCD detector adjacent to the optical

210 microscope of the JEOL-8200 on the sections used for microstructural work. The electron beam was focused on the sections with

211 an accelerating voltage of 15 kV and 30 nA beam current. Black/white digital images were collected with a 40x magnification by

212 beam mapping with the CCD detector at a spatial resolution of 1 μm (beam resolution), which resulted in imaged areas of 27.8 x

213 22.2 mm. The exposure time for image acquisition was 120 s.

214 Petrographic thin sections were later used at the Scanning Electron Microprobe (SEM) to investigate the crystallographic

215 preferred orientation (CPO) of selected sites of the quartz veins from the fault core (sample name TPH-120-4, see Figure

216 2 for sample location). Samples were analysed with a JEOL 6610 SEM equipped with a Nordlys Nano EBSD detector,

217 hosted at the Electron Microscopy Centre of the University of Plymouth, UK. EBSD detailed results are reported in the

218 Supplementary Material.

219 **4 Results**

220 **4.1 BFZ300 fault architecture**

221 The studied BFZ300 section is located at a depth of 426 m b.s.l. and is about 8 m long (Fig. 2a). It strikes NNW-SSE and dips

222 very steeply to subvertically to the southwest (Fig. 2b). It cuts through high-grade veined migmatite, interlayered with gneiss and

223 pegmatitic granite. The fault is a strike-slip fault system formed by two main subparallel fault segments connected by a

224 mesoscopic sinistral step-over zone. Subhorizontal striae defined by elongated trails of chlorite grains and kinematic indicators
225 such as chlorite slickensides (Fig. 2c) and R and R' planes invariably indicate dextral strike-slip kinematics. The most striking
226 mesoscopic characteristic of BFZ300 is the presence in the fault core of a composite set of almost continuous quartz veins
227 (between 1 and 20 cm in thickness) along the entire exposed strike length. A schematic representation of the fault zone is shown
228 in Figure 3.

229 The fault contains a 0.5-2 m thick damage zone separated from the undeformed host rock by two discrete bounding surfaces (Y_I
230 planes according to Tchalenko, 1970 Fig. 2a). The damage zone can be defined in the field on the basis of the presence of a
231 fractured volume containing sets of conjugate dextral and sinistral hybrid fractures (Fig. 3a) intersecting to form a tight acute
232 angle of c. 38° (Figs. 2b, 3a). Laterally continuous, NNW-SSE striking Mode I fractures (joints) invariably bisect this angle (Figs.
233 2b), helping to constrain the stress field orientation at the time of fracture formation, with the greatest compressive stress axis σ_1
234 parallel to the Mode I fracture strike and oriented c. NNW-SSE. Joints are sharp and have a regular spacing of c. 10 cm. The
235 joints and the hybrid fractures of the damage zone contain quartz, referred to as Qtz I hereinafter, forming veins up to 1-1.5 cm
236 thick (Fig. 3a). Fractures and faults decorated by Qtz I have a translucid look that reflect the generally fine grain size of Qtz I (<
237 1 cm, Fig. 3b). Locally they are formed by en-echelon tensional segments connected by shear planes not decorated by any quartz
238 infill (Fig. 3b). Joints occur also as barren fractures defining a penetrative sympathetic fracture cleavage (*sensu* Basson and Viola,
239 2004; green lines in Fig. 2b). Field evidence also suggest that fracture density within the damage zone tends to increase towards
240 the fault core.

241 The fault core is bounded by two main discrete slip surfaces (Y_{II}, Figs. 2a, 3d, f, h). It contains, and is defined by, two distinct
242 generations of quartz veins (Fig. 3c) that are interrupted and offset laterally by a metric sinistral step-over zone (Fig. 3d-f). The
243 main quartz vein of the core is infilled by quartz exhibiting the same mesoscopic appearance of Qtz I in the damage zone; we
244 therefore refer to it as a Qtz I vein. It is accompanied by a younger, subparallel vein formed by a milky-white type of quartz with
245 a significantly larger grain size than Qtz I (>1 cm) that we refer to as Qtz II (Fig. 3c). Locally, pockets of cataclasite and breccia
246 formed at the expense of the host migmatitic gneiss are also observed along and in between the two veins (Figs. 3g, i). The Qtz
247 II vein exhibits a quite irregular, curved geometry (Figs. 3c, h) and a variable thickness up to a maximum of c. 20 cm. The
248 minimum Qtz II vein thickness coincides spatially with an apparent lateral displacement of the vein. The BFZ300 core varies in
249 thickness between 20 and 30 cm along most of the exposed fault length, but becomes thicker (up to 50 cm) in the compressional
250 step-over zone that connects the two fault segments that are offset laterally by c. 1 m. The sinistral step-over zone is defined by
251 synthetic T fractures (Figs. 3d, e) and contains a decimetric brecciated lens (Fig. 3d). T fractures are filled by Qtz I veins (Fig.
252 3e).

253 Chlorite is present as a secondary phase, with a modal abundance between 5 and 10 vol% in both Qtz I and Qtz II veins. In Qtz I
254 veins it occurs as euhedral/subhedral crystals up to 1-2 mm in size (Fig. 3g). Chlorite is present mostly as a disseminated,
255 interstitial phase, concentrated mainly in the internal part of the Qtz I veins (Fig. 3g). In the Qtz II vein, however, it occurs as
256 elongated crystals (5-8 mm in length) arranged perpendicularly to the walls of the vein, which suggests orthogonal dilation at the

257 time of opening (Fig. 3h). The Qtz II vein contains also small (1-2 cm) aggregates of sulphides (sphalerite, pyrite, galena, and

258 chalcopyrite) mainly concentrated in the central part of the vein (Fig. 3g).

259 As observed in the field, the presence of Qtz I veins along the joints in the damage zone and the continuity of the fault core Qtz I

260 vein suggest Mode I fracturing during Qtz I emplacement (Figs. 2a, 3a, c). The semi-continuous parallelism of Qtz I and Qtz II

261 veins in the fault core, combined with the location of the Qtz II vein along the walls of the Qtz I vein, suggest the partial

262 reactivation of the Qtz I vein during Qtz II emplacement. Dilation leading to Qtz II emplacement exploited and further reworked

263 the Qtz I-host rock contact, that seemingly had a lower tensile strength than the pristine migmatite. The reconstructed time

264 relationship between the two vein generations is also consistent with local evidence of the Qtz II vein partly crosscutting the Qtz

265 I vein (Fig. 3f).

266 **4.2 BFZ300 microstructural analysis**

267 To constrain the spatial and temporal association of fault rocks and the type of fluid involved in the deformation, several outcrop

268 samples, each representative of a specific structural domain, were collected (TPH-120-2, TPH-120-3, TPH-120-4, TPH-120-5

269 and TPH-120-6), in addition to samples PH21 and PH22 from diamond drill cores that intersect BFZ300 at the same depth in an

270 area that is currently not excavated. From these samples we prepared 10 petrographic thin sections (samples TPH-120-2, TPH-

271 120-4, TPH-120-6, PH21 and PH22) and 9 doubly-polished sections for fluid inclusion analysis (thickness ~150 μm, samples

272 TPH-120-2, TPH-120-4, TPH-120-6, PH21 and PH22). Due to the extensive reactivation of the fault zone and the consequent

273 obliteration of the FI record, the FI study was carried out only in samples TPH-120-4, TPH-120-6 and PH21. Hand samples and

274 drill cores localities are shown in Figure 3.

275 The microstructural work was carried out on oriented petrographic thin sections cut orthogonally to the migmatitic foliation and

276 parallel to the slickenlines.

277 In the following we provide a description of the microstructural characteristics of BFZ300 by detailing our findings and

278 observations separately for the main structural domains of the fault zone.

279

280 *4.2.1 Damage zone*

281 Qtz I veins within the damage zone cut across the migmatitic host rock and form the infill of conjugate sets of hybrid fractures,

282 which, when studied at the microscale, appear as formed by dilatant segments joined by cataclastic shear fractures (Fig. 4a).

283 Shearing on the latter is well documented by the asymptotic bending into the shear surfaces of foliation planes formed by the

284 alignment of chlorite and muscovite, both partly altered to sericite and chlorite, respectively (Fig .4a). Qtz I infilling the tensional

285 segments has an average grain size between 200 μm and 3 mm and exhibits a rather heterogeneous texture, from purely blocky

286 to mixed elongated-blocky (Figs. 4b, c). The largest crystals (800 μm to 1 mm) are elongated and stretched from the vein walls

287 towards the inner part of the vein (Figs. 4c, 5a). At least two episodes of vein growth/renewed dilation, as indicated by the

288 presence of median lines (ML), are visible within one of the studied veins and confirm a syntaxial growth mechanism for the vein

289 (Fig. 5; e.g. Bons et al., 2012). Medial lines are defined by the alignment of chlorite, sericite, and carbonate aggregates (Figs. 5a,

290 b, d). Blocky euhedral quartz crystals are also found varying in grain size between 300 and 600 µm. These crystals are juxtaposed

291 against very fine grained quartz (<200 µm) within sericite-rich cataclastic bands (Fig. 4b). These cataclasites contain also

292 hydrothermally altered host-rock fragments including pervasively altered K-feldspar-bearing lithic fragments and

293 phyllosilicates.

294 With the exception of the blocky variety, Qtz I crystals exhibit various degrees of crystal-plastic deformation and recovery. They

295 contain widespread evidence of undulose extinction and extinction bands (Fig. 5b), and incipient bulging along grain boundaries

296 is also evident (Fig. 5c). Millimetric intracrystalline barren fractures are also recognized (e.g. Fig. 5c). Cathodoluminescence

297 imaging of Qtz I from the damage zone also shows the presence of a dense network of healed quartz microfractures (Fig. 4d),

298 which demonstrates healing subsequent to brittle deformation and fracturing.

299 Chlorite occurs along the ML of the veins, secondary cracks, along grain boundaries and as as inclusions within quartz crystals.

300 It has a vermicular texture (Fig. 5d) and crystal dimensions up to 50 µm.

301

302 *4.2.2 Fault core*

303 In the fault core, Qtz I grain size reaches the smallest observed value (range: 30-800 µm, Fig. 6a), although it is strongly variable

304 within the vein, suggesting the presence of heterogeneous and complex structural sub-domains. The earliest post-vein

305 emplacement deformation stage is reflected by the low-temperature, intracrystalline deformation of the largest crystals (400-800

306 µm in size). Undulose extinction, wide extinction bands (WEBs, Derez et al., 2015), and bulging along grain boundaries are the

307 most common microstructures ascribable to this deformation stage (Figs. 6a, b). A first brittle deformation event is documented

308 by narrow, intracrystalline fractures that crosscut the largest quartz crystals (Fig. 6c) and which locally contain new grains of

309 quartz ranging in size between 20-100 µm (Fig. 6d). More in detail, these new grains form parallel bands that are oriented at low

310 angle (<30°) to the vein walls and that can be up to 2 mm in length and 200 µm in thickness. Plastically deformed Qtz I crystals

311 hosting these intracrystalline bands of new grains are cut across by another later set of subparallel intercrystalline fractures, which

312 are interpreted as the expression of yet another deformation event that occurred under overall brittle conditions. These fractures

313 are parallel to the strike of BFZ300 and are in turn sealed by partly recrystallized new quartz grains (grain size: 50-150 µm; Fig.

314 6e). The cathodoluminescence imaging of these fractures shows that they are sealed, yielding an homogeneous dark signal (Fig.

315 S1 of the Supplementary Material). They are locally decorated by trails of fluid inclusions (Figs. S2a, d of the Supplementary

316 Material) and can be up to 2.5 cm in length and up to 500 µm in width (Fig. 6a). EBSD maps were acquired along some of these

317 intercrystalline bands, and results suggest that the new grains sealing the fractures reflect the combined effect of initial cracking,

318 grain nucleation and subsequent partial dynamic recrystallization (Figs. S2b, c of the Supplementary Material).

319 Qtz II within the fault core is typically coarse grained (individual crystals: 300 µm-1 cm in size) and exhibits a regular blocky

320 texture devoid of any shape or crystal preferred orientation (Fig. 7a). Locally, these large crystals display primary growth textures,

321 such as primary FIAs oriented parallel to specific crystallographic planes. With the exception of undulose extinction, Qtz II does

not show clear evidence of plastic deformation, although cathodoluminescence imaging of optically continuous Qtz II has also shown that a dense network of healed quartz microfractures locally crosscuts Qtz II crystals (Fig. 7c). These are relatively thin (hundreds of μm thick) networks that are poorly visible to invisible by standard petrographic analysis. The only petrographic evidence for these healed microfractures within quartz are well defined trails of fluid inclusions crosscutting primary growth bands (Fig. 7d).

Chlorite is the second most abundant phase within the fault core Qtz I and Qtz II veins and occurs with a variety of textures. Aggregates of vermicular chlorite similar to that occurring in the damage zone are also present in Qtz I from the core (Fig. 8e), although chlorite with flaky and radiate textures (Fig. 8f) is also present. The latter is generally 100-300 μm in size and is in textural equilibrium with quartz and rare calcite. Radiate chlorite overgrowing fractured Qtz II (Fig. 7b) suggests late Qtz II precipitation.

Associated with Qtz II, a sulphide assemblage made of pyrite, sphalerite, galena and chalcopyrite (Figs. 7d, e, see also Fig. 3g) forms aggregates that are commonly located along quartz grain boundaries. These aggregates have dimensions between 10 and 600 μm.

Multiply reworked breccias and cataclasites occur within and crosscut BFZ300. In the studied sections, a cataclastic band between 5 and 8 mm thick crosscuts both Qtz I and Qtz II veins (Fig. 8a), but is in turn crosscut by a different quartz-radiate chlorite vein displaying evidence of syntaxial growth. This cataclasite contains poorly sorted and angular quartz clasts between 8 and 12 mm in size set in a finer (20-200 μm in size) white mica-quartz matrix. The largest quartz fragments show irregular, lobate grain boundaries and are affected by undulose extinction. We interpret these textures as the product of dissolution and cataclastic reworking of Qtz I..

Parallel sets of stylolitic seams trend c. N-S, parallel to the strike of BFZ300, and mark the two sides of the cataclastic band (Figs. 8a, c). They host anhedral sphalerite, stannite, galena, pyrite, and chalcopyrite (Fig. 8d), which are coeval with the formation of the Qtz II vein. We interpret the presence of these anhedral sulphide minerals along the stylolite as the product of passive concentration by pression-solution.

4.3. Fluid inclusion data

4.3.1 Fluid inclusion petrography

The studied FIAs contain invariably a two-phase fluid (liquid-vapour) and are mainly arranged in secondary trails within Qtz I crystals in the damage zone (Type S1) and also within Qtz I fault core, where they form dismembered (Type S2) trails and also appear as individual clusters inside the crystals affected by crystal-plastic deformation (Type S3). Within Qtz II, FIAs are arranged as pseudosecondary (Type PS) and secondary (Type S4) trails. Representative examples of FI petrographic features are shown for each structural domain in Fig. 9. Table 1 provides a schematic representation of the location of the FI types, in addition to their location within the fault architecture and their fluid properties.

Damage Zone: Within Qtz I grains (Figs. 9a, b), secondary FIAs are found as trails (Fig. 9a) that parallel what we interpret as healed, old microfractures. In these assemblages, FIs have a maximum size between 2 and 20 µm, a regular equidimensional shape (i.e. negative crystal morphology), and a volume fraction, φ ($\varphi = V_v/V_{tot}$, see section 3), ranging between 5 and 15% (Fig. 9b).

Fault Core: Qtz I grains host secondary FIAs (Type S2), which are transgranular trails (Fig. 9c) along healed joints and hybrid fractures. These trails are locally interrupted and dismembered by aggregates of new, fine-grained quartz grains (Fig. 9c), and generate a texture that is indeed typical of Qtz I from the fault core (Fig. 6a). Fluid inclusions vary in size between 1 and 10 µm, have a φ of 10-20%, and show a negative crystal morphology (Fig. 9d). Fluid inclusions are also found as isolated clusters inside intensely recrystallised quartz domains (Fig. 9c). FIAs inside these recrystallized quartz domains were pervasively obliterated during later episodes of ductile deformation. The development of WEBs, intercrystalline bands and bulging resulted in the remobilization (i.e., "transposition" *sensu* Anderson et al., 1990) of these assemblages. This is regularly observed and is documented, for instance, by the presence of short, secondary trails of regularly shaped inclusion oriented at a high angle with respect to a longer, parent trail (Fig. 9c). Morphologically, these trails resemble the transposed trails documented in high-grade metamorphic rocks (Andersen et al., 1990; Van den Kerkhof et al., 2014). Different types of fluid inclusion morphologies are found within the intensely recrystallized quartz domains (Fig. 9f). Negative crystal morphology is observed in some areas of the selected samples, but it is uncommon. More typical is instead the "dismembered" morphology (cf: Vityk and Bodnar, 1995; Tarantola et al., 2010), which is observed in the relatively large inclusions (> 20 µm). This morphology is made of a central (often empty) inclusion, showing several tails and re-entrants, surrounded by three-dimensional clusters of small "satellite" inclusions. These clusters might be arranged with a quasi-planar geometry inside the host (i.e. in a trail-like fashion). Another typical texture found in most assemblages is the "scalloped" morphology of small- to medium-sized inclusions (<10-15 µm), which is defined by the presence of indentations, embayments, irregularities, and sharp tips of the inclusion walls (Fig. 9f). Small inclusions (<1 µm) are also found at the edge of the straight, regular boundaries of new quartz grains; they are mostly dark, i.e. they are vapour-rich or empty, and are equant in shape (Fig. 9e). Although small inclusions do not allow a microtermometric study of the fluid-phase behaviour in this structural domain, they confirm the complex reactivation history of BFZ300.

Qtz II contains both pseudosecondary (Type PS) and secondary (Type S4) assemblages (Figs. 9g, i, h). The first type is arranged in trails that cut at low angle the hosting quartz but not the neighbouring phases (e.g. chlorite). In these assemblages, FIs are relatively large (2-45 µm) and exhibit elongated shape and φ values between 15 and 30 % (Fig. 9 g). Type S4 FIAs (Fig. 9h) host two-phase inclusions whose size (5-35 µm) is similar to that of PS trails, but show a φ between 30 and 40 % (Fig. 9 i).

Primary FIAs are also present along growth planes of Qtz II, where they have a relatively large size (20-50 µm; Figs. S3a, b, c of the Supplementary Material). They present irregular and dismembered textures, which suggest intense post-entrapment re-equilibration.

In summary, our microtextural study shows that the FIAs to be selected for the microthermometric study are only those hosted within Qtz I and Qtz II crystals with little to no recrystallization and whose inclusions have textures corresponding to the least

387   intense post-entrapment re-equilibration (Bodnar, 2003b and references therein; Tarantola et al., 2010). These are the

388   pseudosecondary and secondary FIAs in which dendritic or transposed inclusions are absent, and in which the host quartz exhibits

389   only undulose extinction (S1, S2, S4 and PS).

390

391   *4.3.2 Microthermometry*

392   *Damage Zone:* Secondary FIAs hosted within Qtz I from the damage zone (Type S1) show a range of Tm_{ice} between -5.9 and -

393   0.1 °C, which corresponds to a salinity of 0-9 wt% NaCleq (Fig. 10a). In these FIAs, final homogenization (Th_{tot}) occurs into the

394   liquid phase (i.e. by disappearance of the vapour bubble) and mainly between 150-400 °C (Fig. 10e).

395   *Fault Core:* The secondary FIAs hosted within Qtz I in the fault core (Type S2) show a range of Tm_{ice} between -8.2 and -0.4 °C,

396   which corresponds to salinities between 0 and 14 wt% NaCleq (Fig. 10b), and final homogenization occurs into the liquid phase

397   between 130 and 410 °C (Fig. 10f).

398   Pseudosecondary FIAs entrapped within Qtz II (Type PS) show a range of Tm_{ice} between -13.6 and -0.1 °C, which corresponds

399   to a salinity range between 0 and 18 wt% NaCleq (Fig. 10c); final homogenization occurs into the liquid phase and is comprised

400   between 150 and 440 °C (Fig. 10g). Secondary FIAs in Qtz II (Type S4) show a range of Tm_{ice} between -11 and 0 °C, which

401   corresponds to a 0-15 wt% NaCleq range of salinity (Fig. 10d), while final homogenization into the liquid phase is comprised

402   between 130 and 430 °C (Fig. 10h).

403   As no gases were determined during microthermometric analysis (i.e. melting of carbonic phase or clathrate hydrates were not

404   detected during the freezing experiments), additional micro Raman analysis was performed on a set of representative FIAs

405   (samples: TPH-120-4; TPH-120-6; PH21; PH22). Aqueous fluid inclusions hosted both by the Qtz I and Qtz II show peaks at the

406   characteristic wavenumbers of CH_4 (2917 cm-1). and CO_2 (1388 cm-1). These peaks were determined as weak in all spectra, and

407   CO_2 detection was sporadic in a few inclusions of only one sample of the fault core (TPH-120-4). Although spectroscopic

408   detections, the CO_2- and CH_4-bearing inclusions are not systematically associated with specific quartz vein generations or

409   microstructures (i.e. intracrystalline healed cracks, WEB's planes, intercrystalline fractures). We cannot therefore associate the

410   presence of CO_2 and/or CH_4 to any specific deformation stage of the fault.

411   Such spectroscopic determinations are consistent with the lack of microthermometric evidence of carbonic phase or clathrate

412   hydrates during the freezing experiments (cf. Rosso and Bodnar, 1995; Dubessy et al., 2001). The impossibility to detect CO_2-

413   and CH_4-bearing fluids during the freezing experiments indicate a gas pressure that is systematically lower than that required to

414   observe clathrate dissociation (e.g., 1.4 MPa in CO_2-H_2O fluids, Rosso and Bodnar, 1995), i.e. it shows low gas concentrations.

415   As a consequence, we have modelled the fluid phases as simple H_2O-NaCl systems..

416   **4.4 Chlorite and sulphide geothermometry**

417   Chlorite composition has been determined for several generations of chlorites in association with Qtz I and II, namely vermicular

418   chlorite associated with Qtz I from the damage zone, vermicular and radiate chlorite associated with Qtz I from the fault core,

and radiate chlorite associated with Qtz II from the fault core (Table 2). Chlorite compositions are shown in Figure 11a and are expressed as function of the Fe/(Fe+Mg) ratio. Chlorite compositional data are presented according to the structural domain of the fault they are associated with and to the corresponding texture. Vermicular chlorite associated with Qtz I in the damage zone has a XFe range between 0.50 and 0.55, while vermicular chlorite associated with Qtz I from the fault core has a XFe of 0.53. Radiate chlorite associated with Qtz I from the fault core has a XFe range between 0.71 and 0.81 while radiate chlorite associated with Qtz II from the fault core is between 0.65 and 0.80, constraining compositions within the ripidolite and aphrusiderite end-members.

Temperature-composition relationships for the quartz-chlorite pair portrayed in the T-R^{2+}–Si diagram of Bourdelle and Cathelineau (2015) show that, in the hypothesis of quartz-chlorite equilibrium, the precipitation of vermicular chlorite within the Qtz I of the damage zone took place in the 175-240 °C range (green diamonds of Fig. 11a). This range is distinct from that of the vermicular and radiate chlorite from Qtz I of the fault core, which is probably c. 350 °C because the measured R^{2+}–Si compositional parameters (R^{2+} = Mg+Fe) plot at the edge of, or slightly outside, the calibrated region of the Bourdelle and Cathelineau plot (red diamonds of Fig. 11a). We stress that the high-T chlorite plots parallel to the 350 °C isotherm, suggesting that it precipitated most probably at the same, or at a similar, temperature. Radiate chlorite associated with Qtz II from the fault core is instead compatible with an equilibrium precipitation at 160-220 °C (light-blue diamonds in Fig. 11a).

The collected EPMA data show that the sulphides associated with Qtz II have compositions that approach those of pure phases (Table 3). Pyrite has trace element concentrations (Cu, As, Pb, Ni, Zn) that are in general below the EPMA detection limit, while galena, sphalerite, and chalcopyrite show only some significant trace contents of Fe and Zn (e.g., Fe: 0.22-1.00 wt% in galena; Zn: 0.11-3.95 wt% in chalcopyrite). Pyrite and sphalerite from the Qtz II veins (Fig. 7e) have trace element concentrations that are, again, mostly below detection limits.

The stylolites bordering the cataclasite bands described above and formed at the contact between the Qtz I and Qtz II vein contain pyrite, galena, and the sphalerite-stannite pair (Figs. 8a, c, d), with the latter showing the largest compositional variation. This pair represents a mineral geothermometer because the partitioning of Zn and Fe between sphalerite and stannite was demonstrated to be temperature dependent but pressure independent (Nekrasov et al., 1979; Shimizu and Shikazono, 1985). In the fourteen analysed pairs, stannite shows a range of Zn concentrations varying between 0.48 wt% and 3.25 wt%, while those of Fe, Cu and Sn vary within narrow ranges (Fe: 12.74±0.56 wt%; Cu: 28.30 ±0.33 wt%; Sn: 27.65 ±0.71 wt%). Sphalerite in the pair has concentrations of Fe and Zn of 7.63±0.87 wt% and 56.68 ±1.17 wt%, respectively. These ranges allow the calculation of the partition coefficient (K_D) of the reaction: Cu_2FeSnS_4 (in stannite) + ZnS (in sphalerite) = Cu_2ZnSnS_4 (in stannite) + FeS (in sphalerite). We have used the $logK_D$–T relationship of Shimizu and Shikazono (1985) to calculate the formation temperature of the pair, which is portrayed in the ($X_{Cu2FeSnS4}/X_{Cu2ZnSnS4}$)-($X_{FeS}/X_{ZnS}$) plot of Shimizu and Shikazono (Fig. 11b). The resulting 220-305 °C interval lies at the low end of, or slightly outside, the 250-350 °C interval of the geothermometer.

Therefore, we consider the 250-305 °C interval as the best estimation of the formation T of sphalerite-stannite in the stylolite.

5 Discussion

Our work constrains the architecture and the environmental conditions at which BFZ300 deformation took place. Field and petrographic observations support the idea of transiently elevated fluid pressures, cyclic frictional-viscous deformation and progressive, yet discrete strain localization (Figs. 2, 3). Analytical data suggest that these deformation cycles took place at the BDTZ. In the following, we discuss these constraints by systematically considering our different analytical results.

5.1. Fluid inclusion data and mineral-pair geothermometry

Field evidence combined with microstructural observations, fluid inclusion analyses and the documented distinct generations of synkinematic chlorites confirm that Qtz I and Qtz II veins precipitated from distinct batches of aqueous fluid (i.e. H_2O-NaCl), that ingressed the fault zone during different stages of its evolution.

We documented a wide range of bulk salinity for each FIAs entrapped within the quartz veins in each structural domain (Figs. 10a-d). This suggests post-entrapment re-equilibration of fluid inclusions (cf. Bakker and Jansen, 1990; Diamond et al., 2010). The Th_{tot} varies between c. 130 and 440 °C without a clear mode or a skew (Figs. 10eh) indicating that no common range of entrapment temperature can be identified in the dataset. Therefore, we conclude that even the properties of petrographically intact FIAs do not correspond to chemically well-preserved assemblages. Indeed, the ranges of Th_{tot} in individual FIAs are typically of the order of 150-200 °C (Figs. 10e-h), i.e. a value that is much higher than the ~10 °C range expected for homogeneous FIAs entrapped isochorically and isoplethically (Fall et al., 2009; Vityk and Bodnar, 1998) and that demonstrates post-entrapment re-equilibration (cf. Vitik and Bodnar, 1998; Bodnar, 2003b; Sterner and Bodnar, 1989; Invernizzi et al., 1998). A major implication of fluid inclusion re-equilibration in our study is that the calculated fluid properties do not rigorously reflect those of the pristine fluid originally entrapped within BFZ300, but rather that of a fluid that modified its properties during the fault activity.

Then, a possible approach to interpret our FI dataset is the comparison with the experimental work on synthetic fluid inclusions subjected to a range of post-entrapment re-equilibration conditions (Bakker, 2017; Bakker and Jansen, 1990, 1991, 1994; Vityk and Bodnar, 1995, 1998; Vityk et al., 1994; Invernizzi et al., 1998). A straight comparison to the experiments is in our case difficult because most experimental work was carried out at high TP conditions (500-900 °C; 90-300 MPa) and also only few experiments were carried out under deviatoric stress conditions that approach those of natural rocks (Diamond et al., 2010; Tarantola et al., 2010). Despite these limitations, however, some key experimental results provide fundamental constraints on our dataset. First, both hydrostatic and uniaxial compression experiments showed that in each re-equilibrated FIA a number of inclusions survive virtually intact the modified post-entrapment PT conditions, showing that only severe deformation brings to total re-equilibration and complete obliteration of pristine inclusions (i.e., $\Delta\sigma$>100 MPa in uniaxial compression experiments; >400 MPa change of confining P in hydrostatic experiments). Second, under conditions leading to only low to moderate re-equilibration, the bulk chemical composition of the fluid inclusions does not change significantly from that of the pristine inclusions.

483 All of this implies that natural quartz samples with microstructures typical of moderate T deformation, such as deformation

484 lamellae, deformation bands, undulose extinction and bulging, and hosting FIAs with moderately re-equilibrated textures, should

485 still contain a number of inclusions whose properties resemble those of the pristine fluid. In this scenario, our microthermometric

486 dataset can be used to constrain the more probable salinity ranges of the fluid batches which trigger BZ300 reactivation stages.

487 Two possible interpretations of the microthermometric dataset can be follow and we can give accordingly different salinity ranges

488 for the fluids.

489 One possibility is that the different quartz veins and the fluids trapped within fluid inclusions originated from multiple pulses of

490 a single, low salinity fluid, with a salinity between 0 and 7 wt%NaCleq, as shown by the distribution of >70% of the bulk salinities

491 skewed towards values of 7 wt% NaCleq or less (Fig. 10a-d). Thus, it is possible that aliquots of the 0-7 wt% NaCleq FIAs from

492 Qtz I and II crystals from both the damage zone and fault core is still representative of the pristine sampled fluid. These inclusions

493 would be those that survived or were relatively less affected by deformation events postdating their entrapment. Inclusions falling

494 outside the most typical 0-7wt% NaCleq salinity range would instead correspond to those which progressively modified their

495 properties as a consequence of fluid-rock interaction during faulting and that experienced significant H_2O loss and consequent

496 salinity increase during the successive stages of fault deformation (cf. Bakker and Jansen, 1990; Diamond et al., 2010). The large

497 documented range of Th_{tot} lacking a specific mode observed in individual FIAs is the product of fluid density changes caused by

498 fluid inclusion re-equilibration during post-entrapment deformation. This would have happened repeatedly and cyclically within

499 the host quartz during all ductile and brittle stages of deformation of the multi-stage deformation history of BFZ300.

500 Alternatively, multiple batches of fluids with different salinities (from low to intermediate salinity) may have ingressed and

501 evolved within BFZ300 during its activity. In fact, considering the salinity dataset presented for each structural domain, fluid

502 salinity can be seen clustering in restricted ranges typical for each domain: 1) the salinity of 60% of secondary fluid inclusions in

503 Qtz I from the damage zone is between 0 and 1 wt%NaCleq; 2) > 80% of the secondary inclusions in Qtz I from the fault core

504 preserve a salinity in the 1 to 5 range wt%NaCleq; 3) 75% of pseudosecondary inclusions in Qtz II show salinity values between

505 6 and 11 wt%NaCleq and 4) ~70% of the secondary inclusions trapped within Qtz II show salinity values between 0 and 3

506 wt%NaCleq. These clusters may best represent the original compositional ranges of different batches of fluids, each involved

507 during a different faulting stage. Salinities outside these clusters may instead be explained again as resulting from the post-

508 entrapment re-equilibration of those fluids with different salinities. This hypothetical scenario, in which chemically distinct fluids

509 ingressing the fault and interacting with the rock at different times (e.g. Selverstone et al., 1992; Boiron et al., 2003; Famin et al.,

510 2005) is also reinforced by several lines of observation such as: the variation of chlorite composition, the slight change in

511 paragenesis/redox state with Qtz II and Qtz I (i.e. the absence of massive sulphides in Qtz I) and by the prolonged history of

512 faulting (see below).

513 Fully aware of the interpretative uncertainties of our dataset, we have combined the microthermometric data of the studied FIAs

514 with the independent quartz-chlorite and sphalerite-stannite geothermometers to constrain the most probable fluid pressure during

515 the faulting events. With this approach, we use the formation temperatures of the mineral pairs as independent geothermometers

516 and consider the intersection between these values and the FIA isochores to derive the ranges of trapping pressure (cf. Roedder

517 and Bodnar, 1980). In Figure 12, we present the ranges of the possible pressure (P_f) of the fluids involved during faulting as

518 calculated by combining the fluid inclusion data with the constraints provided by the pair-mineral geothermometry and the hydro-

519 and lithostatic pressure gradients and a possible geothermal gradient (e.g. Van Noten et al., 2011; Selverstone et al., 1995; Jaques

520 and Pascal, 2017). The reconstructed regional gradients at the time of vein emplacement are derived from peak metamorphic

521 conditions (4-5 kbar; 650-700 °C leading to c. 40 °C/km; from Kärki and Paulamäki, 2006). Hydrostatic and lithostatic pressures

522 are then calculated by using pure water density and assuming a rock density of 2700 kgm^{-3}, respectively. These gradients are used

523 to constrain the upper and lower bounds to physically possible fluid pressures. We computed the maximum and minimum

524 isochores by using the entire salinity and Th_{tot} ranges obtained from the FIAs in each structural domain (Fig. 10). We also

525 computed the isochores of the inclusions with the most representative salinity estimates for each structural domain obtained by

526 comparing the frequency diagrams (Fig. 10) with the Th_{tot} vs. salinity plots (Supplementary Material Fig. S4). Considering the

527 peak temperature of each structural zone from the geothermometric estimations in combination with the computed isocores, the

528 estimated peak conditions of the fluid pressure are: 1) 80 MPa for Qtz I from the damage zone, 2) 210 MPa for Qtz I from the

529 fault core; 3) 140 MPa from pseudosecondary inclusions in Qtz II from the core and 4) 180 MPa from secondary inclusions in

530 Qtz II, still from the core (Fig. 12; Table 1).

531 In addition to the P_f peak conditions we can also constrain the physically possible fluid pressure ranges for each stage of fluid

532 ingress, which are derived by considering the temperature range estimated for each structural domain. Thus, for the damage zone,

533 a P_f interval of 50-80 MPa (Fig. 12a) can be derived by intersecting the range of T obtained from the chlorite-quartz pair in the

534 Qtz I from the damage zone with the range of isochores from the same quartz. As to the fault core, we combine the 350 °C

535 constraint from the chlorite-quartz pair from Qtz I in the fault core with the isochores from the same quartz, which yields P_f

536 between c. 30 and 210 MPa (Fig. 12b). Similarly, the intersection between the equilibrium T of the sphalerite-stannite pair in the

537 Qtz II from the fault core and the range of isochores of the pseudosecondary FIAs of Qtz II defines P_f values between 50 and 140

538 MPa (Fig. 12c). Estimations from secondary FIAs in Qtz II constrain a range between 40 and 180 MPa (Fig. 12d).

539 As also supported by the microstructures described above, we propose that these values are sufficiently accurate to constrain at

540 least four stages of fault reactivation, each triggered by a fluid with distinct physical and compositional properties.

541 As shown by the T vs. P plots of Figure 12, the secondary FIAs entrapped in Qtz I from the damage zone constrain the lowest

542 value of P_f (i.e. 50-80 MPa) of the entire dataset. We interpret this not as representative of the early BFZ300 localization, but

543 rather as possibly resulting from fluid entrapment during a later stage of fault reactivation at T ~200 °C. This is also consistent

544 with the calculated temperature of crystallization of the vermicular chlorite associated with Qtz I from the damage zone (175-240

545 °C, Fig. 11b) and with the secondary nature of the entrapped FIAs. Also, the most abundant salinities observed in the Qtz I from

546 the damage zone (0-1 wt%NaCleq) coincide with the lowest Th_{tot} measured in the same structural domain. Later fracturing of Qtz

547 I in the damage zone may thus have been coeval with the formation of vermicular chlorite preserved therein, which is found along

548 secondary cracks and median lines (Fig. 5d).

549   In light of these considerations, we propose that initial BFZ300 localization occurred in the presence of a fluid with T and P of at

550   least 350 °C and 210 MPa, respectively. Later faulting continued by cyclic brittle-ductile switches induced and assisted by fluid

551   batches at progressively lower temperature and pressure.

552 **5.2. Structural evolution and fluid flow: a conceptual model**

553   Based on the integration of field, microstructural, thermometric and fluid inclusions constraints (Table 1), we propose a

554   conceptual model for the structural evolution of BFZ300 (Fig. 13). The fault's finite strain results from several slip episodes

555   mediated by multiple events of fluid ingress and fluid-rock interaction. A first constraint provided by our study is that the analysis

556   of the bulk chemical composition of the fluids that ciclycally ingressed the fault suggests the likely presence of several batches

557   of fluids of varying salinity and composition.

558   The embrittlement of the Olkiluoto metamorphic basement (time t_1 of Figs. 13a, b) represents the initial stage of the deformational

559   history of BFZ300, when conditions for brittle dilation and fracturing of the Paleoproterozoic basement were first met in a

560   transient fashion. We propose that brittle failure under still ductile environmental conditions was caused by transiently elevated

561   P_f (> 210 MPa), as also demonstrated by field evidence of hydrofracturing (pure tensional en enchelon veins at the BDTZ depth).

562   Hydrofracturing of the host basement is also indicated by the emplacement of Qtz I veins within the diffuse network of joints and

563   conjugate hybrid/shear fractures of the damage zone (Figs. 13a, 3a, b). These brittle features are quite broadly distributed

564   suggesting an initial volumetrically diffuse strain distribution. Their formation caused the overall mechanical weakening of the

565   host rock volume, which in turn facilitated later strain localization. Brittle structures formed during this stage are discordant to

566   the ENE-WSW striking metamorphic foliation (Fig. 1b), which they cut at high angle (Fig. 13a). Conditions for tensional and

567   hybrid failure require low differential stress, i.e. σ_1- $\sigma_3 \sim$ 4T, where T is the tensional strength of the rock. Opening of fractures

568   caused a stress drop, sudden increase of permeability, fluid venting and inhibited further build-up of P_f. Dilatant fractures were

569   partially infilled by Qtz I, which precipitated from a first fluid, with inferred low salinity (in the range between 1 and 5

570   wt%NaCleq). Precipitation of Qtz I and formation of veins within these fractures caused hardening of the system. The progressive

571   recovery of shear stresses altered the overall background stress conditions such that failure, after causing initial pure dilation, was

572   later accommodated by hybrid extensional - and, eventually, by shear fracturing (Fig. 13b), thus forming laterally continuous and

573   interconnected shear fractures associated with breccia pockets and cataclasites (Figs. 3d, g, i). Conjugate shear fractures connected

574   the previously formed extensional fractures through fracture coalescence (e.g. Griffith, 1921; Sibson, 1996; Fig. 13a). At the

575   micro-scale this is demonstrated by the elongated blocky texture of Qtz I crystals from the damage zone (Figs. 4c and 5a), where

576   crystals grew at high angle to the vein boundaries (thus suggesting initial near-orthogonal dilation) and are physically connected

577   by cataclastic shear bands to form a fault-fracture mesh (e.g. Sibson, 1996). Cataclastic bands formed at the expense of the

578   migmatitic host rock are enriched in authigenic, synkinematic sericite, likely due to the interaction between K-feldspar and fluids

579   circulating in the dilatant fault zone (Fig. 4b). Shear fractures thus deformed the migmatitic host rock to connect dilatant and

580   mostly Qtz I-filled tension gashes during a continuum of deformation. The conjugate shear fractures ascribable to this stage

581 invariably define tight acute angles (Figs. 2b, 3a), which we take as further evidence of overall low differential stress conditions
582 at the time of failure (Fig. 13b).
583 In synthesis, Qtz I veins from the damage zone are interpreted as the expression of the earliest stage of fault nucleation, before
584 strain localization affected a progressively narrower rock volume to eventually form the main fault core. Indeed, the meso- and
585 microscale features observed in Qtz I-damage zone, lacking of pervasive crystal-plastic deformation as otherwise occurred in Qtz
586 I-fault core, are used to document the initial stage of embrittlement. Based on geometric, kinematic and deformation style
587 characteristics, we tentatively assign this deformation episode to Stage 1 by Mattila and Viola (2014, their Fig. 18), i.e. to a
588 discrete brittle episode considered the expression of the earliest onset of brittle conditions in southwestern Finland c. 1.75 Ga ago,
589 under overall NW-SE to NNW-SSE transpressive conditions.
590 Further deformation of the BFZ300 (time t_2 of Fig. 13c) occurred by progressive inward strain localization and narrowing of the
591 actively deforming volume of the deformation zone (from a wide damage zone to a narrow fault core). The early BFZ300 core,
592 consisting of the main Qtz I vein is interpreted as having formed at this stage, within an overall dextral strike-slip kinematic
593 framework. Emplacement of the Qtz I vein in the core represents the last pulse of this brittle deformational episode (Fig. 13b).
594 Major fluid venting was likely associated with it, such that the system, once brittle failure in the core had occurred by
595 hydrofracturing, moved back to a more diffuse deformation style typical of the still prevailing ductile conditions. Microscopic
596 evidence of crystal-plastic deformation and dynamic recrystallization (Figs. 6a, b; Table 1) overprinting the early brittle structures
597 of Qtz I in the fault core supports slow strain rate conditions during deformation. However, this ductile background deformation
598 was punctuated by renewed and cyclically transient embrittlement as documented by healed fractures shown by trails of secondary
599 fluid inclusions cutting across both the ductile fabrics and the earlier brittle deformational features (Figs. 6c, S2a, b). EBSD
600 analysis of the new grains documented along healed microcracks also suggests that they likely nucleated from fluids circulating
601 in the early fractures before being later deformed in the low-temperature plasticity regime. Thus, we show that at the BDTZ
602 'neocrystallisation' by nucleation and growth in fractured fragments and dynamic recrystallisation (typically by bulging and
603 subgrain rotation) coexist and compete in the overall microstructural evolution of quartz (e.g. Kjøll et al., 2015). Repeated fluid
604 ingresses and related deformation would, in addition, also have caused some of the post-entrapment equilibration of the FI, as
605 discussed above.
606 Mattila and Viola (2014) described a second brittle stage (referred to as Stage 2, their Fig. 18) during which a c. N-S to NNE-
607 SSW-oriented episode of transpressional deformation affected southwestern Finland. Geometric and temporal relationships
608 between structures of Stages 1 and 2 (see also Viola et al., 2009) were used to infer a clockwise rotation of the horizontal
609 compression direction from NW-SE (Stage 1) to NNE-SSW (Stage 2). Consistent with the kinematic framework of Stage 2, we
610 propose here that during progressive regional exhumation and cooling to entirely brittle conditions, the BFZ300 deformation
611 continued through a further, distinct deformation phase (t_3 of Fig. 13e). This stage accommodated the selective reactivation of the
612 BFZ300 core, with renewed dilation due to the rotated σ_1 during Stage 2 acting subparallel to the strike of the Qtz I vein in the
613 BFZ300 core. Localised dilation in a still fluid-rich system allowed the emplacement of the Qtz II vein (Fig. 13e). Our estimations
614 indicate peak conditions of P_f 140 MPa and T ≈ 305° C. The BFZ300 core was reactivated by an intermediate salinity fluid (in

the range between 6 and 11 wt%NaCleq) under overall hybrid conditions (Fig. 13f), as suggested by the irregular thickness and curved geometry of the Qtz II vein therein, and by the synkinematic chlorite crystals that are stretched orthogonally to the vein boundaries (Fig. 3h). The Qtz II vein invariably localized along at the contact between Qtz I and the host rock (Figs. 3f, 13e) suggesting selective reactivation along the pre-existing principal slip zones, which represented the weakest part of the fault (Fig. 13h). Evidence for mesoscale hybrid fracturing and our P_f estimates (Fig. 12) suggest that P_f was lower than that of the earlier deformation stages during Qtz I emplacement.

BFZ300 underwent one or more events of brittle fracturing and induration (Fig. 13g), as suggested by the CL imaging of Qtz II crystals (Fig. 7c). The fluid pressure peak value for this structural stage is c. 180 MPa.

A possible, very late reactivation stage of unknown age is also documented by the secondary chlorite associated with Qtz I in the damage zone (Figs. 5a, d). Also, the stylolitic seams striking parallel to BFZ300 fault zone suggest compression oriented c. E-W, i.e. subparallel to the inferred Sveconorwegian main shortening direction (e.g., Viola et al., 2011). The sphalerite-stannite mineral pairs arranged along these structures were possibly concentrated through a pression-solution during this deformational stage.

Skyttä and Torvela (2018) proposed that the BFZ300 is a brittle structure localized onto a zone of incomplete structural transposition inherited from the earlier ductile history of the Olkiluoto basement. However, in our mesoscale and microstructural analysis we did not find evidence of any ductile precursor, and we note that BFZ300 cuts the ductile structural grain at high angle, which excludes any reactivation of precursor ductile fabrics.

5.3. Implications for seismic deformation at the base of the BDTZ

This study demonstrates the role of overpressured fluids on strain localisation during the incipient stages of fault nucleation and subsequent reactivation(s) at the BDTZ. The maximum estimated fluid pressure and fluid temperature conditions derived in this study (peak conditions of 210 MPa and 350 °C) are indeed realistic for the base of the seismogenic zone in the continental lithosphere (e.g., Scholz, 1990, and references therein) where the brittle-ductile transition for quartz occurs.

Mechanical models of long-term deformation (Rolandone and Jaupart, 2002) propose that deformation at the brittle-ductile transition can be reasonably described as being mostly accommodated by intermittent and concomitant coseismic slip and ductile flow. Hydrofracturing, as that documented in this study by the Qtz I and II veins, is possibly related in that context to seismic failure. Faults accommodating hydrofracturing are indeed commonly interpreted as seismogenic (e.g. Sibson, 1992a; Cox, 1995) particularly at depth.

Our study confirms this view because BFZ300 contains not only brittle fault rocks overprinting and overprinted by veins, but also clearcut evidence of mutually overprinting brittle and ductile deformation (Fig. 6). In light of the field observations discussed and of the constraints derived, we suggest therefore that BFZ300 behaved in a seismic way at least during the emplacement of the principal Qtz I and Qtz II veins. In this perspective, two possible scenarios can be considered to explain the genetic relationships between BFZ300 and a possible seismic behaviour of the crust during the Svecofennian orogeny. In a first scenario, the quartz veins of the fault core would represent the result of coseismic rupture during the mainshocks of a fully developed seismic cycle.

647   Pore pressure fluctuations caused the repeated transient embrittlement of the rock mass, which was otherwise under overall ductile

648   conditions. The documented brittle-ductile cycles are thus the expression of coseismic fracturing and aseismic creep between the

649   individual shocks, as shown by viscous deformation overprinting the brittle features, guided by the residual differential stress.

650   A second possibility is that faulting occurred in the absence of a well-defined sequence of main- and aftershocks. As in the case

651   of man-induced earthquakes triggered by high-pressure fluids during injection of fluids (e.g. Healy et al., 1968), where

652   deformation is typically accommodated by diffuse swarms of low magnitude seismicity rather than well-defined mainshock-

653   aftershock sequences (Cox, 2016), we propose that BFZ300 might have localised strain by diffuse veining with crack and seal

654   textures (Cox, 2016). Breccias and cataclasites (Figs. 3, 8) mutually overprinting with veins show that failure and veining were

655   indeed broadly coeval (e.g. Cox, 1995; Cox, 2016). Healing in fluid-rich environments can occur over short periods of time (days-

656   months) when compared with recurrence time of large earthquakes (10-100 years) (Olsen et al., 1998; Tenthorey and Cox, 2006).

657   Therefore, the documented repeated switches between brittle and ductile deformations would then be steered again by transient

658   episodes of fluid overpressuring but in this case would express the accommodation of swarms of minor background earthquakes

659   within overall ductile conditions.

660   Microstructures of fault-rocks exhumed from the brittle-ductile transition in other geological settings, are mostly in agreement

661   with our hypotheses of seismic deformation. Transient and short term high-stress deformation followed by phases of stress

662   relaxation, which is prevalently characterized by recovery and recrystallization processes, has been documented by several

663   authors in deformed quartz (Trepmann and Stöckhert, 2003; Trepmann et al., 2007; Bestmann et al., 2012; Trepmann and

664   Stöckhert, 2013; Trepmann et al., 2017).

665   6 Conclusions

666   This study shows that a multi-scale and multi-technique approach leading to the generation of independent constraints offers the

667   potential to reconstruct in detail the evolutionary history of also fault zones that have experienced multiple events of reactivation

668   triggered by fluid overpressure and in which intense fluid-rock re-equilibration processes have taken place. We document the

669   localised, initial embrittlement of the Paleoproterozoic basement of southwestern Finland at the BDTZ, which occurred by brittle

670   failure under overall ductile conditions in response to transiently high fluid pressure and temperature (peak conditions: $P_f >$ 210

671   MPa; T~350 °C). Our results further constrain the importance of cyclic seismicity and fluids in the fragmentation of Precambrian

672   cratons when deformed at the BDTZ, something that is not yet that well understood for the Fennoscandian Shield. Our study,

673   moreover, provides potentially important inputs to many modern geological applications, including site characterization of deep

674   geological disposal facilities for spent nuclear fuel. Results from the detailed geological characterization of faults at the Olkiluoto

675   site can thus be used toward the continuous updating of the geological site description and yield further constraints on the

676   mechanics of faulting at the BDTZ.

677

678

679   ACKNOWLEDGMENTS

680   This research was funded by Posiva Oy. We thank Oliver Vanderhaeghe and two anonymous reviewers for their constructive

681   reviews, which led to a greatly improved manuscript. Stephen F. Cox, Michael Stipp and Alfons M. Van den Kerkhof are all

682   warmly thanked for fruitful discussions during the early stages of this work. Danilo Bersani and Andrea Risplendente are also

683   thanked for their help with the Raman and SEM analyses.

References

685   Aaltonen, I., Lahti, M., Engström, J., Mattila, J., Paananen, M., Paulamäki, S., Gehör, S., Kärki, A., Ahokas, T., Torvela,
686   T. and Front, K.: Geological model of the Olkiluoto site, Version 2.0, Posiva Working Report 2010- 70, Posiva Oy,
687   Eurajoki, 2010.

688   Aaltonen, I., Engström, J., Front, K., Gehör, S., Kosunen, P. and Kärki, A.: Geology of Olkiluoto. Posiva Working Report
689   2016- 16., Posiva Oy, Eurajoki., 2016.

690   Andersen, T., Austrheim, H. and Burke, E. A. J.: Fluid inclusions in granulites and eclogites from the Bergen Arcs,
691   Caledonides of W. Norway, Mineral. Mag., 54, 145–158, 1990.

692   Ault, A. K. and Selverstone, J.: Microtextural constraints on the interplay between fluid-rock reactions and deformation,
693   Contrib. to Mineral. Petrol., 156(4), 501–515, doi:10.1007/s00410-008-0298-9, 2008.

694   Bakker, R.: Re-Equilibration Processes in Fluid Inclusion Assemblages, Minerals, 7(7), 117, doi:10.3390/min7070117,
695   2017.

696   Bakker, R. J. and Jansen, J. B. H.: Preferential water leakage from fluid inclusions by means of mobile dislocations, Nature,
697   345(6270), 58–60, doi:10.1038/345058a0, 1990.

698   Bakker, R. J. and Jansen, J. B. H.: Experimental post-entrapment water loss from synthetic CO2-H2O inclusions in natural
699   quartz, Geochim. Cosmochim. Acta, 55(8), 2215–2230, doi:10.1016/0016-7037(91)90098-P, 1991.

700   Bakker, R. J. and Jansen, J. B. H.: A mechanism for preferential H2O leakage from fluid inclusions in quartz, based on
701   TEM observations, Contrib. to Mineral. Petrol., 116(1–2), 7–20, doi:10.1007/BF00310686, 1994.

702   Basson, I. J. and Viola, G.: Passive kimberlite intrusion into actively dilating dyke-fracture arrays: Evidence from fibrous
703   calcite veins and extensional fracture cleavage, Lithos, 76(1–4 SPEC. ISS.), 283–297, doi:10.1016/j.lithos.2004.03.041,
704   2004.

705   Bestmann, M., Pennacchioni, G., Nielsen, S., Göken, M. and de Wall, H.: Deformation and ultrafine dynamic
706   recrystallization of quartz in pseudotachylyte-bearing brittle faults: A matter of a few seconds, J. Struct. Geol., 38, 21–38,
707   doi:10.1016/j.jsg.2011.10.001, 2012.

708   Bodnar, R. J.: The origin of fluid inclusions, in: Samson, I., Anderson, A. & Marshall, D. (eds.) Fluid inclusions: Analysis
709   and Interpretation. Vancouver, Canada: Mineralogical Association of Canada, 11-18, 2003a.

710   Bodnar, R. J.: Re-equilibration of fluid inclusions, in: Samson, I., Anderson, A. & Marshall, D. (eds.) Fluid inclusions:

711 Analysis and Interpretation. Vancouver, Canada: Mineralogical Association of Canada, 213-230, 2003b.

712 Boiron, M., Cathelineau, M., Banks, D. A., Fourcade, S. and Vallance, J.: Mixing of metamorphic and surficial fluids
713 during the uplift of the Hercynian upper crust : consequences for gold deposition, Chem. Geol., 194, 119–141, 2003.

714 Bons, P. D.: The formation of large quartz veins by rapid ascent of fluids in mobile hydrofractures, Tectonophysics, 336(1–
715 4), 1–17, doi:10.1016/S0040-1951(01)00090-7, 2001.

716 Bons, P. D., Elburg, M. A. and Gomez-Rivas, E.: A review of the formation of tectonic veins and their microstructures, J.
717 Struct. Geol., 43, 33–62, doi:10.1016/j.jsg.2012.07.005, 2012.

718 Bourdelle, F. and Cathelineau, M.: Low-temperature chlorite geothermometry: a graphical representation based on a a T–
719 R2+–Si diagram, Eur. J. Mineral., 27(5), 617–626, doi:10.1127/ejm/2015/0027-2467, 2015.

720 Caine, J. S., Evans, J. P. and Forster, C. B.: Fault zone architechture and permeability structure, Geology, 24(11), 1025–
721 1028, doi:10.1130/0091-7613(1996)024<1025, 1996.

722 Compton, K. E., Kirkpatrick, J. D. and Holk, G. J.: Cyclical shear fracture and viscous flow during transitional ductile-
723 brittle deformation in the Saddlebag Lake Shear Zone, California, Tectonophysics, 708, 1–14,
724 doi:10.1016/j.tecto.2017.04.006, 2017.

725 Cox, S. F.: Faulting processes at high fluid pressures: An example of fault valve behavior from the Wattle Gully Fault,
726 Victoria, Australia, J. Geophys. Res., 100(B7), 841–859, 1995.

727 Cox S. F.: Coupling between deformation, fluid pressures and fluid flow in ore-producing hydrothermal environments,
728 Econ. Geol., 100th Anniversary Volume, 39–75, 2005.

729 Cox, S. F.: Injection-driven swarm seismicity and permeability enhancement: Implications for the dynamics of
730 hydrothermal ore systems in high fluid-flux, overpressured faulting regimes - An invited paper, Econ. Geol., 111(3), 559–
731 587, doi:10.2113/econgeo.111.3.559, 2016.

732 Cox, S., Knackstedt, M., & Braun, J.: Principles of structural control on permeability and fluid flow in hydrothermal
733 systems, Reviews in Econ. Geol., 14, 1-24, 2001.

734 Crider, J. G. and Peacock, D. C. P.: Initiation of brittle faults in the upper crust: A review of field observations, J. Struct.
735 Geol., 26(4), 691–707, doi:10.1016/j.jsg.2003.07.007, 2004.

736 De Paola, N., Collettini, C., Trippetta, F., Barchi, M. R. and Minelli, G.: A mechanical model for complex fault patterns
737 induced by evaporite dehydration and cyclic changes in fluid pressure, J. Struct. Geol., 29(10), 1573–1584,
738 doi:10.1016/j.jsg.2007.07.015, 2007.

739 Derez, T., Pennock, G., Drury, M. and Sintubin, M.: Low-temperature intracrystalline deformation microstructures in
740 quartz, J. Struct. Geol., 71, 3–23, doi:10.1016/j.jsg.2014.07.015, 2015.

741 Diamond, L. W.: Introduction to gas-bearing, aqueous fluid inclusions, in : Fluid Inclusions: Analysis and Interpretation,
742 edited by: I. Samson, A. Anderson, D. Marshall, eds., 363–372., 2003.

743 Diamond, L. W., Tarantola, A. and Stünitz, H.: Modification of fluid inclusions in quartz by deviatoric stress. II:
744 Experimentally induced changes in inclusion volume and composition, Contrib. to Mineral. Petrol., 160(6), 845–864,
745 doi:10.1007/s00410-010-0510-6, 2010.

746 Dubessy, J., Buschaert, S., Lamb, W., Pironon, J. and Thiéry, R.: Methane-bearing aqueous fluid inclusions: Raman
747 analysis, thermodynamic modelling and application to petroleum basins, Chem. Geol., 173(1–3), 193–205,
748 doi:10.1016/S0009-2541(00)00275-8, 2001.

749 Ehlers, C., Lindroos, A. and Selonen, O.: The late Svecofennian granite-migmatite zone of southern Finland-a belt of
750 transpressive deformation and granite emplacement., Precambrian Res., 64(1–4), 295–309, 1993.

751 Fall, A., Donald, R. and Bodnar, R. J.: The effect of fluid inclusion size on determination of homogenization temperature
752 and density of liquid-rich aqueous inclusions, Am. Mineral., 94(11–12), 1569–1579, doi:10.2138/am.2009.3186, 2009.

753 Famin, V., Hébert, R., Philippot, P. and Jolivet, L.: Evolution of hydrothermal regime along a crustal shear zone , Tinos
754 Island , Greece, Tectonics, 23, doi:10.1029/2003TC001509, 2004.

755 Famin, V., Hébert, R., Phillippot, P. and Jolivet, L.: Ion probe and fluid inclusion evidence for co-seismic fluid infiltration
756 in a crustal detachment, Contrib. Mineral Petrol., 150, 354–367, doi:10.1007/s00410-005-0031-x, 2005.

757 Garofalo, P. S.: Mass transfer during gold precipitation within a vertically extensive vein network (Sigma deposit - Abitibi
758 greenstone belt - Canada). Part II. Mass transfer calculations, Eur. J. Mineral., 16(5), 761–776, doi:10.1127/0935-
759 1221/2004/0016-0761, 2004.

760 Garofalo, P. S., Matthäi, S. K. & Heinrich, C. A.: Three-dimensional geometry, ore distribution, and time-integrated mass
761 transfer through the quartz-tourmaline-gold vein network of the Sigma deposit (Abitibi belt - Canada), Geofluids, 2, 217-
762 232, 2002.

763 Garofalo, P. S., Fricker, M. B., Günther, D., Bersani, D. and Lottici, P.: Physical-chemical properties and metal budget of
764 Au-transporting hydrothermal fluids in orogenic deposits, Geol. Soc. London, Spec. Publ., 402(1), 71–102,
765 doi:10.1144/SP402.8, 2014.

766 Goddard, J. V. and Evans, J. P.: Chemical changes and fluid-rock interaction in faults of crystalline thrust sheets,
767 northwestern Wyoming, U.S.A., J. Struct. Geol., 17(4), 533–547, doi:10.1016/0191-8141(94)00068-B, 1995.

768 Goldstein, R. H. and Reynolds, T. J.: Fluid Inclusion Microthermometry, Syst. Fluid Inclusions Diagenetic Miner., 87–
769 121, doi:10.2110/scn.94.31.0087, 1994.

770 Gorbatschev, R. and Bogdanova, S.: Frontiers in the Baltic Shield, Precambrian Res., 64(1–4), 3–21, doi:10.1016/0301-
771 9268(93)90066-B, 1993.

772 Griffith, A. A.: The Phenomena of Rupture and Flow in Solids, Philos. Trans. R. Soc. london, 221(582–893), 163–198,
773 1920.

774 Guermani, A. and Pennacchioni, G.: Brittle precursors of plastic deformation in a granite: An example from the Mont Blanc
775 massif (Helvetic, western Alps), J. Struct. Geol., 20(2–3), 135–148, doi:10.1016/S0191-8141(97)00080-1, 1998.

Healy, J. H., Rubey, W. W., Griggs, D. T. and Raleigh, C. B.: The Denver Earthquakes. Disposal of waste fluids by injection into a deep well has riggered earthquakes near Denver, Colorado., Science, 161(3848), 1301–1310, 1968.

Heinrich, C. A., Andrew, A. S., and Knill, M. D.: Regional metamorphism and ore formation: Evidence from stable isotopes and other fluid tracers, Reviews in Econ Geol, 11, 97–117, 2000.

Hey, M. H.: A new review of the chlorites., Mineral. Mag. J. Mineral. Soc., XXX(224), 1954.

Hudson, J. A. and Cosgrove, J.: Geological History and Its Impact on the Rock Mechanics Properties of the Olkiluoto Site, Posiva Working Report 2006, Posiva Oy, Eurajoki, 2006.

Invernizzi, C., Vityk, M., Cello, G. and Bodnar, R.: Fluid inclusions in high pressure/low temperature rocks from the Calabrian Arc (Southern Italy): the burial and exhumation history of the subduction-related Diamante-Terranova unit, J. Metamorph. Geol., 16, 2, 247–258, 1998.

Jaques, L. and Pascal, C.: Full paleostress tensor reconstruction using quartz veins of Panasqueira Mine, central Portugal; part I: Paleopressure determination, J. Struct. Geol., 102, 58–74, doi:10.1016/j.jsg.2017.07.006, 2017.

Kaduri, M., Gratier, J. P., Renard, F., Çakir, Z. and Lasserre, C.: The implications of fault zone transformation on aseismic creep: Example of the North Anatolian Fault, Turkey, J. Geophys. Res. Solid Earth, 122(6), 4208–4236, doi:10.1002/2016JB013803, 2017.

Kerrich, R.: Some effects of tectonic recrystallisation on fluid inclusions in vein quartz, Contrib. to Mineral. Petrol., 59(2), 195–202, doi:10.1007/BF00371308, 1976.

Kjøll, H. J., Viola, G., Menegon, L. and Sørensen, B. E.: Brittle-viscous deformation of vein quartz under fluid-rich lower greenschist facies conditions, Solid Earth, 6(2), 681–699, doi:10.5194/se-6-681-2015, 2015.

Kohlstedt, D. L., Evans, B. and Mackwell, S. J.: Strength of the lithosphere: Constraints imposed by laboratory experiments, J. Geophys. Res., 100(B9), 587–602, 1995.

Korja, A., Heikkinen, P. and Aaro, S.: Crustal structure of the northern Baltic Sea palaeorift, Tectonophysics, 331(4), 341–358, doi:10.1016/S0040-1951(00)00290-0, 2001.

Kukkonen, I. T. and Lauri, L. S.: Modelling the thermal evolution of a collisional Precambrian orogen: High heat production migmatitic granites of southern Finland, Precambrian Res., 168(3–4), 233–246, doi:10.1016/j.precamres.2008.10.004, 2009.

Kärki, A. and Paulamäki, S.: Petrology of Olkiluoto, Posiva Report 2006-02, Posiva Oy, Eurajoki., 2006.

Lahtinen, R. and Survey, G.: Palaeoproterozoic tectonic evolution of the Fennoscandian Shield. In: Lehtinen, M., Nurmi, P.A., Rämö (eds.), Precambrian Geology of Finland: Key to the Evolution of the Fennoscandian Shield, Developments in Precambrian Geology, 2005.

Mancktelow, N. S. and Pennacchioni, G.: The influence of grain boundary fluids on the microstructure of quartz-feldspar mylonites, J. Struct. Geol., 26, 47-69, doi:10.1016/S0191-8141(03)00081-6, 2004.

808 Mancktelow, N. S. and Pennacchioni, G.: The control of precursor brittle fracture and fluid-rock interaction on the
809 development of single and paired ductile shear zones, J. Struct. Geol., 27(4), 645–661, doi:10.1016/j.jsg.2004.12.001, 2005.

810 Mattila, J. and Viola, G.: New constraints on 1.7Gyr of brittle tectonic evolution in southwestern Finland derived from a
811 structural study at the site of a potential nuclear waste repository (Olkiluoto Island), J. Struct. Geol., 67(PA), 50–74,
812 doi:10.1016/j.jsg.2014.07.003, 2014.

813 Menegon, L., Pennacchioni G., Malaspina N., Harris K., and Wood E.: Earthquakes as Precursors of Ductile Shear Zones
814 in the Dry and Strong Lower Crust, Geochem. Geophy. Geosy., 18(12), doi: 10.1002/2015GC006010, 2017.

815 Menegon, L., Marchesini, B., Prando, F., Garofalo, P. S., Viola, G., Anderson, M.and Mattila, J.: Brittle-viscous
816 oscillations and different slip behaviours in a conjugate set of strike-slip faults, Geophysical Research Abstracts Vol. 20,
817 EGU2018-14799, 2018.

818 Miller, S. A.: The Role of Fluids in Tectonic and Earthquake Processes, edited by R. Dmowska, Elsevier., 2013.

819 Mittempergher, S., Dallai, L., Pennacchioni, G., Renard, F. and Di Toro, G.: Origin of hydrous fluids at seismogenic depth:
820 Constraints from natural and experimental fault rocks, Earth Planet. Sci. Lett., 385, 97–109,
821 doi:10.1016/j.epsl.2013.10.027, 2014.

822 Moritz, R., Ghazban, F. and Singer, B. S.: Eocene Gold Ore Formation at Muteh, Sanandaj-Sirjan Tectonic Zone, Western
823 Iran: A Result of Late-Stage Extension and Exhumation of Metamorphic Basement Rocks within the Zagros Orogen, Econ.
824 Geol., 101, 1–28, 2006.

825 Morrison, J.: Meteoric water-rock interaction in the lower plate of the Whipple Mountain metamorphic core complex ,
826 California, J. Metamorph. Geol.,12, 827–840, 1994.

827 Morrison, J. and Anderson, J. L.: Footwall Refrigeration Along a Detachment Fault : Implications for the Thermal
828 Evolution of Core Complexes, Science, 279(January), 63–67, 1998.

829 Mulch, A., Mine, I. De, Cosca, M. A., Mine, I. De, Lausanne, D., Lausanne, C.-, Poincare, H. and Gr, U. M. R.:
830 Reconstructing paleoelevation in eroded orogens, , (6), 525–528, doi:10.1130/G20394.1, 2004.

831 Nekrasov, I. J., Sorokin, V. I. and Osadchii, E. G.: Fe and Zn partitioning between stannite and sphalerite and its application
832 in geothermometry., Phys. Chem. Earth, 11(C), 739–742, doi:10.1016/0079-1946(79)90069-7, 1979.

833 Oliver, N. H. S. and Bons P. D.: Mechanisms of fluid flow and fluid–rock interaction in fossil metamorphic hydrothermal
834 systems inferred from vein–wallrock patterns, geometry and microstructure, Geofluids, 137–162, 2001.

835 Olsen, M. P., Scholz, C. H. and Léger, A.: Healing and sealing of a simulated fault gouge under hydrothermal conditions:
836 Implications for fault healing, J. Geophys. Res., 103(B4), 7421, doi:10.1029/97JB03402, 1998.

837 Pennacchioni, G., Di Toro, G., Brack, P., Menegon, L. and Villa, I. M.: Brittle-ductile-brittle deformation during cooling
838 of tonalite (Adamello, Southern Italian Alps), Tectonophysics, 427(1–4), 171–197, doi:10.1016/j.tecto.2006.05.019, 2006.

839 Roedder, E. and Bodnar, R. J.: Geologic determinations from fluid inclusion studies., Annu. Rev. Earth Planet. Sci.,
840 8(1953), 263–301, 1980.

Rolandone, F. and Jaupart, C.: The distributions of slip rate and ductile deformation in a strike-slip shear zone, Geophys. J. Int., 148(2), 179–192, doi:10.1046/j.1365-246X.2002.01574.x, 2002.

Rosso, K. M. and Bodnar, R. J.: Microthermometric and Raman spectroscopic detection limits of CO2 in fluid inclusions and the Raman spectroscopic characterization of CO2, Geochim. Cosmochim. Acta, 59(19), 3961–3975, doi:10.1016/0016-7037(95)94441-H, 1995.

Scheffer, C., Tarantola, A., Vanderhaeghe, O., Rigaudier, T. and Photiades, A.: CO 2 flow during orogenic gravitational collapse : Syntectonic decarbonation and fl uid mixing at the ductile-brittle transition, Chem. Geol., 450, 248–263, doi:10.1016/j.chemgeo.2016.12.005, 2017a.

Scheffer, C., Tarantola, A., Vanderhaeghe, O., Voudouris, P., Rigaudier, T., Photiades, A., Morin, D. and Alloucherie, A.: The Lavrion Pb-Zn-Fe-Cu-Ag detachment-related district (Attica , Greece): Structural control on hydrothermal flow and element transfer-deposition, Tectonophysics, 717, 607–627, doi:10.1016/j.tecto.2017.06.029, 2017b.

Selverstone, J., Axen, G. J., Bartley, J. M: Fluid inclusion constraints on the kinematics of footwall uplift beneath the Brebber Line normal fault, estern Alps, Tectonics, 14(2), 264-278, 1995.

Selverstone, J., Franz, G., Thomas, S. and Getty, S.: Fluid variability in 2 GPa eclogites as an indicator of fluid behavior during subduction, Contrib to Mineral and Petrol, 112(2-3), 341-357, 1992.

Shimizu, M. and Shikazono, N.: Iron and zinc partitioning between coexisting stannite and sphalerite: a possible indicator of temperature and sulfur fugacity, Miner. Depos., 20, 314–320, 1985.

Scholz, C. H.: The Mechanics of Earthquakes and Faulting, Cambridge: Cambridge University Press, 1990.

Sibson, R. H.: Earthquake faulting as a structural process, J. Struct. Geol., 11(1–2), 1–14, doi:10.1016/0191-8141(89)90032-1, 1989.

Sibson, R. H.: Fault-valve behavior and the hydrostatic-lithostatic fluid pressure interface, Earth Sci. Rev., 32(1–2), 141–144, doi:10.1016/0012-8252(92)90019-P, 1992a.

Sibson, R. H.: Implications of fault-valve behaviour for rupture nucleation and recurrence., Tectonophysics, 211(1–4), 283–293., 1992b.

Sibson, R. H.: Load-strengthening versus load-weakening faulting, J. Struct. Geol., 15(2), 123–128, doi:10.1016/0191-8141(93)90090-W, 1993.

Sibson, R. H.: Structural permeability of fluid-driven fault-fracture meshes, J. Struct. Geol, 18(8), 1996.

Sibson, R. H., Robert, F. and Poulsen, K. H.: High-angle reverse faults, fluid-pressure cycling, and mesothermal gold-quartz deposits, Geology, 16(June 1988), 551–555, doi:10.1130/0091-7613(1988)016<0551:HARFFP>2.3.CO;2, 1988.

Siebenaller, L., Boiron, M. C., Vanderhaeghe, O., Hibsch, C., Jessell, M. W., Andre-Mayer, A. S., France-Lanord, C. and Photiades, A.: Fluid record of rock exhumation across the brittle-ductile transition during formation of a Metamorphic Core Complex (Naxos Island, Cyclades, Greece), J. Metamorph. Geol., 31(3), 313–338, doi:10.1111/jmg.12023, 2013.

873 Siebenaller, L., Vanderhaeghe, O., Jessell, M., Boiron, M. C. and Hibsch, C.: Syntectonic fluids redistribution and
874 circulation coupled to quartz recrystallization in the ductile crust (Naxos Island, Cyclades, Greece), J. Geodyn., 101, 129–
875 141, doi:10.1016/j.jog.2016.07.001, 2016.

876 Skyttä, P. and Torvela, T.: Brittle reactivation of ductile precursor structures: The role of incomplete structural transposition
877 at a nuclear waste disposal site, Olkiluoto, Finland, J. Struct. Geol., 0–1, doi:10.1016/j.jsg.2018.06.009, 2018.Spruzeniece,
878 L. and Piazolo, S.: Strain localization in brittle-ductile shear zones: Fluid-abundant vs. fluid-limited conditions (an example
879 from Wyangala area, Australia), Solid Earth, 6(3), 881–901, doi:10.5194/se-6-881-2015, 2015.

880 Steele-MacInnis, M., Lecumberri-Sanchez, P. and Bodnar, R. J.: HokieFlincs_H2O-NaCl: A Microsoft Excel spreadsheet
881 for interpreting microthermometric data from fluid inclusions based on the PVTX properties of H2O-NaCl, Comput.
882 Geosci., 49, 334–337, doi:10.1016/j.cageo.2012.01.022, 2012.

883 Sterner, S. M. and Bodnar J.: Synthetic fluid inclusions - VII. Re-equilibration of fluid inclusions in quartz during
884 laboratory-simulated metamorphic burial and uplift, J. Metamorph. Geol., 7, 243–260, 1989.

885 Suominen, V.: The chronostratigraphy of southern Finland, with special reference to Postjotnian and Subjotnian diabases.
886 Bull. Geol. Surv. Finl,. 356, 100, 1991.

887 Tarantola, A., Diamond, L. W. and Stünitz, H.: Modification of fluid inclusions in quartz by deviatoric stress I:
888 Experimentally induced changes in inclusion shapes and microstructures, Contrib. to Mineral. Petrol., 160, 825–843,
889 doi:10.1007/s00410-010-0509-z, 2010.

890 Tchalenko, J. S.: Similarities between Shear Zones of Different Magnitudes, Geol. Soc. Am. Bull., 81(6), 1625–1640,
891 doi:10.1130/0016-7606(1970)81[1625:SBSZOD]2.0.CO;2, 1970.

892 Tenthorey, E. and Cox, S. F.: Cohesive strengthening of fault zones during the interseismic period: An experimental study,
893 J. Geophys. Res. Solid Earth, 111(9), 1–14, doi:10.1029/2005JB004122, 2006.

894 Trepmann, C. A. and Stöckhert, B.: Quartz microstructures developed during non-steady state plastic flowat rapidly
895 decaying stress and strain rate, J. Struct. Geol., 25(12), 2035–2051, doi:10.1016/S0191-8141(03)00073-7, 2003.

896 Trepmann, C. A. and Stöckhert, B.: Short-wavelength undulatory extinction in quartz recording coseismic deformation in
897 the middle crust – An experimental study, Solid Earth, 4(2), 263–276, doi:10.5194/se-4-263-2013, 2013.

898 Trepmann, C. A., Stöckhert, B., Dorner, D., Moghadam, R. H., Küster, M. and Röller, K.: Simulating coseismic
899 deformation of quartz in the middle crust and fabric evolution during postseismic stress relaxation - An experimental study,
900 Tectonophysics, 442(1–4), 83–104, doi:10.1016/j.tecto.2007.05.005, 2007.

901 Trepmann, C. A., Hsu, C., Hentschel, F., Döhler, K., Schneider, C. and Wichmann, V.: Recrystallization of quartz after
902 low-temperature plasticity – The record of stress relaxation below the seismogenic zone, J. Struct. Geol., 95, 77–92,
903 doi:10.1016/j.jsg.2016.12.004, 2017.

904 Van den Kerkhof, A., Kronz, A. and Simon, K.: Deciphering fluid inclusions in high-grade rocks, Geosci. Front., 5(5),
905 683–695, doi:10.1016/j.gsf.2014.03.005, 2014.

906 Van Noten, K., Muchez, P. and Sintubin, M.: Stress-state evolution of the brittle upper crust during compressional tectonic

inversion as defined by successive quartz vein types (High-Ardenne slate belt , Germany), J. Geol. Soc. London, 168(2004), 407–422, doi:10.1144/0016-76492010-112.Stress-state, 2011.

Viola, G., Mancktelow, N. S. and Miller, J. A.: Cyclic frictional-viscous slip oscillations along the base of an advancing nappe complex: Insights into brittle-ductile nappe emplacement mechanisms from the Naukluft Nappe Complex, central Namibia, Tectonics, 25(3), 1–20, doi:10.1029/2005TC001939, 2006.

Viola, G., Venvik Ganerød, G. and Wahlgren, C. H.: Unraveling 1.5 Ga of brittle deformation history in the Laxemar-Simpevarp area, southeast Sweden: A contribution to the Swedish site investigation study for the disposal of highly radioactive nuclear waste, Tectonics, 28(5), 1–29, doi:10.1029/2009TC002461, 2009.

Viola, G., Mattila, J., Zwingmann, H., Todd, A. and Raven, M.: Structural and K / Ar Illite Geochronological Constraints on the Brittle Deformation History of the Olkiluoto Region, Southwest Finland, Posiva Working Report 2011, Posiva Oy, Eurajoki, 2011.

Viola, G., Scheiber, T., Fredin, O., Zwingmann, H., Margreth, A. and Knies, J.: Deconvoluting complex structural histories archived in brittle fault zones, Nat. Commun., 7, 1–10, doi:10.1038/ncomms13448, 2016.

Vityk, M. O. and Bodnar, R. J.: Textural evolution of synthetic fluid inclusions in quartz during reequilibration, with applications to tectonic reconstruction, Contrib. to Mineral. Petrol., 121(3), 309–323, doi:10.1007/BF02688246, 1995.

Vityk, M. O. and Bodnar, R. J.: Statistical microthermometry of synthetic fluid inclusions in quartz during decompression reequilibration, Contrib. to Mineral. Petrol., 132(2), 149–162, doi:10.1007/s004100050413, 1998.

Vityk, M. O., Bodnar, R. J. and Schmidt, C. S.: Fluid inclusion as a tectonothermobarometers: Relation between pressure-tempreture history and reequilibration morphology during crystal thickening, Geology, 22, 731–734, doi:10.1130/0091-7613(1994)022<0731:FIATRB>2.3.CO, 1994.

Wehrens, P., Berger, A., Peters, M., Spillmann, T. and Herwegh, M.: Deformation at the frictional-viscous transition: Evidence for cycles of fluid-assisted embrittlement and ductile deformation in the granitoid crust, Tectonophysics, 693, 66–84, doi:10.1016/j.tecto.2016.10.022, 2016.

Wilkins, R. W. T. and Barkas, J. P.: Fluid inclusions, Deformation and Recrystallization in Granite Tectonites, Contrib. Mineral. Petrol., 65, 293-299, 1978.

934
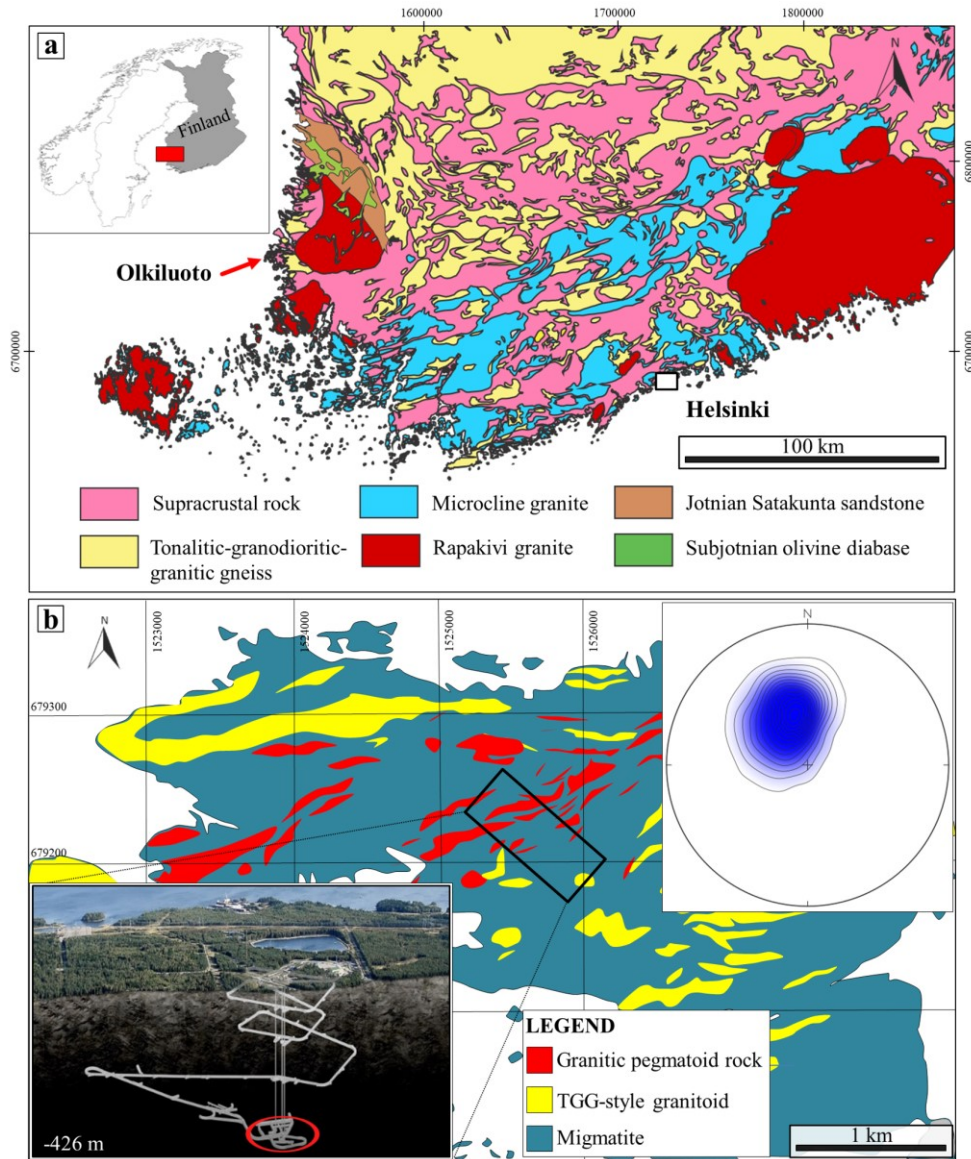
Figure 1. (a) Simplified geological map of southwestern Finland modified after Mattila and Viola (2014). (b) Geological sketch of the Olkiluoto
Island. The upper right inset shows the poles to foliation planes measured from all available Olkiluoto drill cores (N = 4479, equal area, lower
hemisphere projection; Mattila and Viola, 2014). The lower left inset is a panoramic photograph with an overlay drawing of the underground
infrastructure (photo courtesy of Posiva Oy, Finland). The red circle shows the depth location of BFZ300. Coordinates are given in the local
KKJ1 coordinate system.
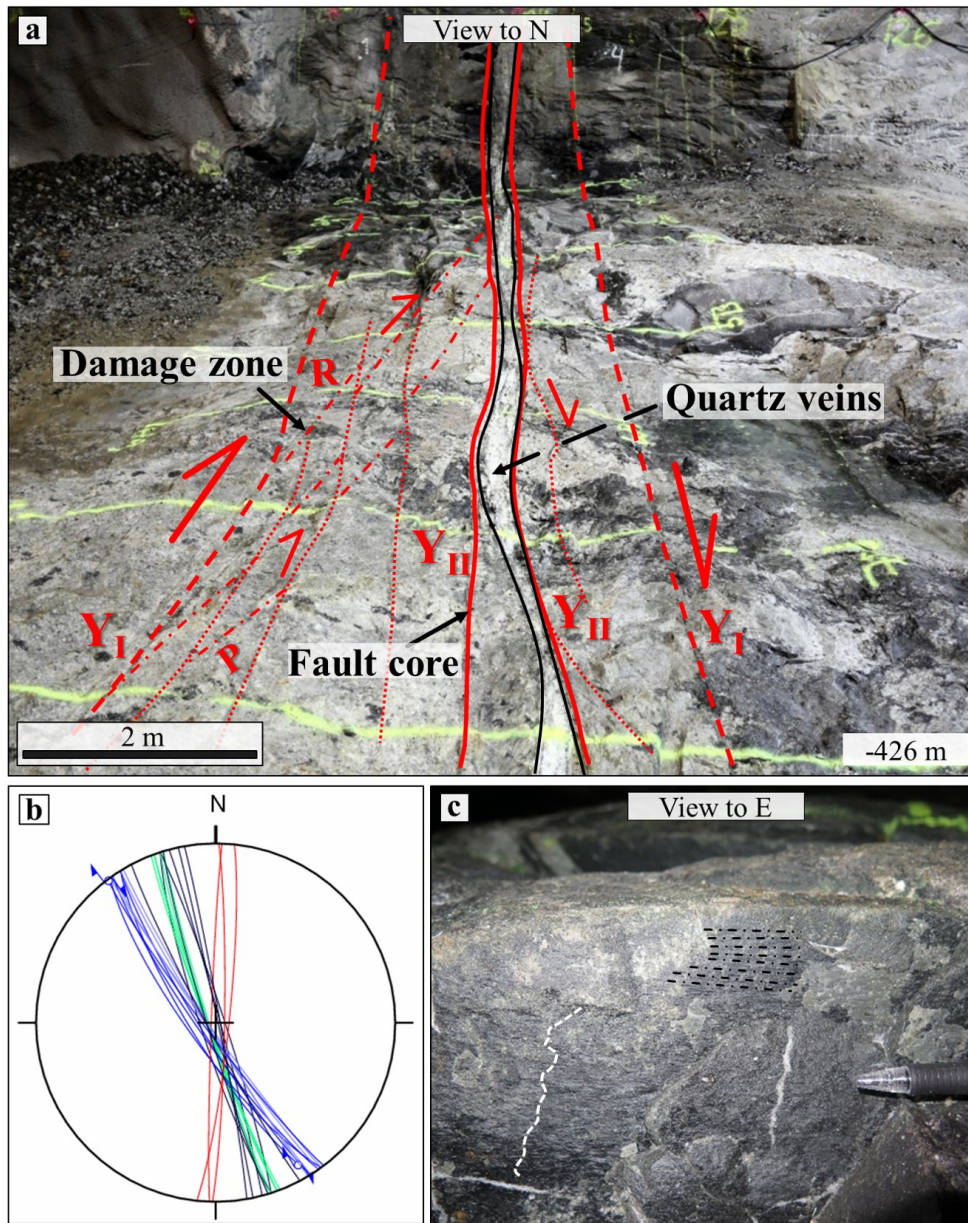
940
941 Figure 2. (a) View to the north and interpretation of the structural elements of BFZ300. (b) Lower-hemisphere, equiangular projection of
942 conjugate fault segments (blue great circles: dextral faults; red great circles: sinistral faults), cleavage (green great circles) and Qtz I-chlorite
943 veins infilling joints (black great circles). (c) Slickensides (white dashed line) and slickenlines (black dashed lines) on a chlorite-decorated, NW-
944 SE striking fracture plane at the vein-host interface indicating dextral strike-slip kinematics.
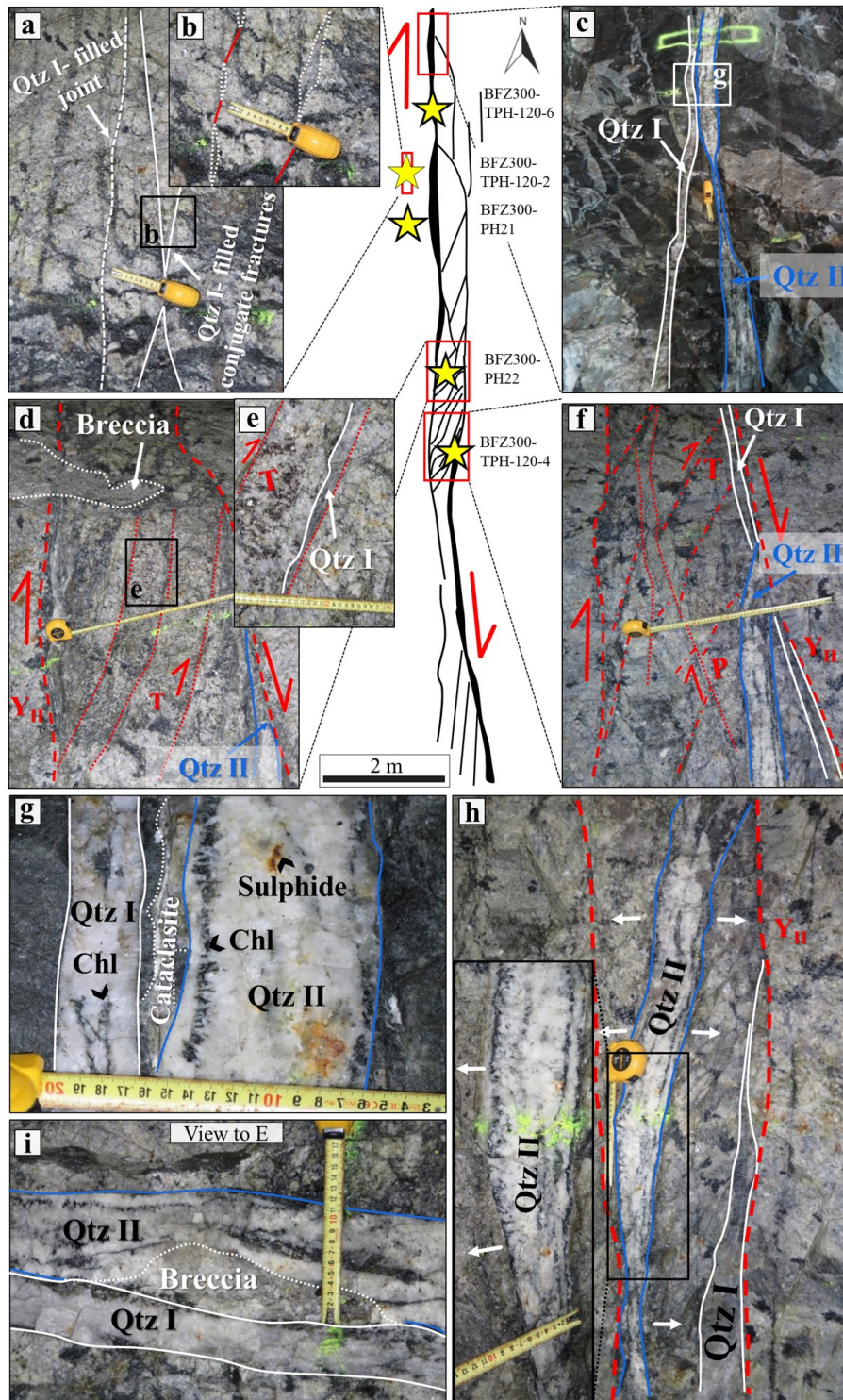
Figure 3. BFZ300 architecture with examples of representative structural features. The red rectangles locate the areas where detailed outcrop photos were taken. Stars locate hand and drill core samples. Stars with a black outline identify samples used for the microthermometric study. Note that the fault is made of two main segments offset laterally at a sinistral compressive step-over zone. Fault core quartz veins are shown by thicker black lines in the schematic model (centre of figure), while blue and white lines highlight the positions of the two types of quartz veins in the outcrop pictures. (a) Damage zone made of mm-thick, en-echelon veins connected by conjugate shear segments. (b) Detail of (a) showing fractures filled by the first quartz generation (Qtz I). (c) Two distinct generations of quartz-chlorite veins recognised in the fault core (Qtz I and Qtz II). (d) Detail of the sinistral compressional step-over zone characterized by multiple and parallel T fractures, filled by Qtz I. A brecciated body is crosscut by the Y planes. (e) Tensional fracture infilled by Qtz I. (f) Compressional structures (P shears) from the step-over zone and relationships between Qtz I and Qtz II. The Riedel geometry suggests that the Qtz II vein formed due to the reactivation of the internal principal slip zones (Y_{II}). Note the Qtz II vein cutting the Qtz I vein. (g) Juxtaposed Qtz I and Qtz II veins. Qtz I veins are thinner and made of a translucid, small grained quartz. In contrast, Qtz II veins, which contain pockets of sulphide aggregates, are thicker and made of larger and euhedral quartz. Chlorite occurs as minor phase in both veins. Notice the presence of a cataclastic band between the two veins. (h) Spatial continuity of the chlorite aggregates within the Qtz II veins, which grow always orthogonal to the vein boundaries. This open space filling texture suggests hybrid conditions of reactivation of the older Qtz I veins. (i) Small quartz breccia formed between the two generations of quartz veins.

960
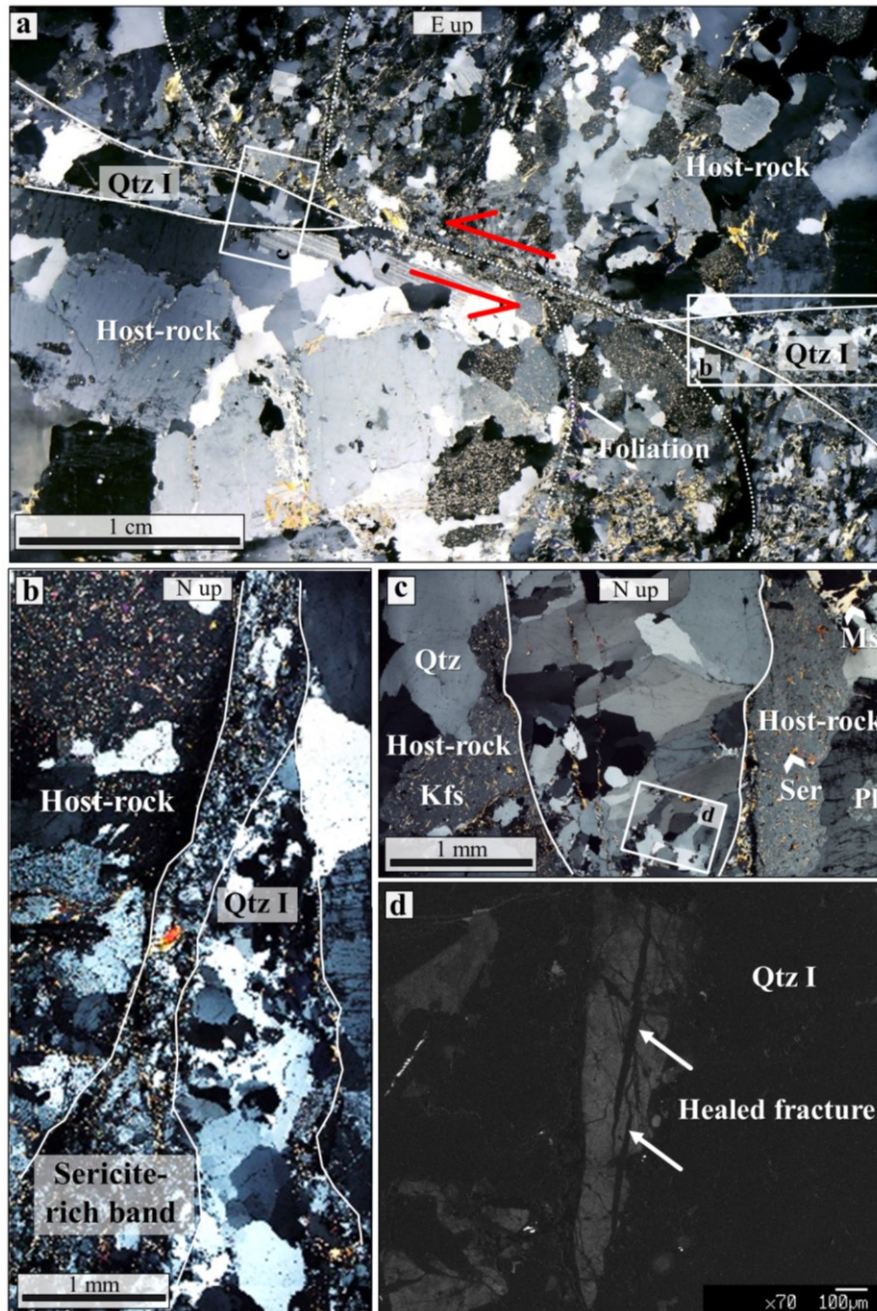
Figure 4. Microtextural characteristics of Qtz I from the damage zone of BFZ300 (sample: TPH-120-2). (a) Stitched photomicrographs of a Qtz I vein interconnecting with a sinistral shear band (crossed nicols). Faulting kinematics is suggested by drag folds in the host rock. (b) Tip of Qtz I vein hosted by a sericite-rich cataclastic band of the host rock. (c) Detail of panel a showing open-space filling texture in the Qtz I vein. Notice the sericite microfractures crosscutting Qtz I. (d) Panchromatic cathodoluminescence image of Qtz I showing healed microfractures crosscutting the crystal.

966
967
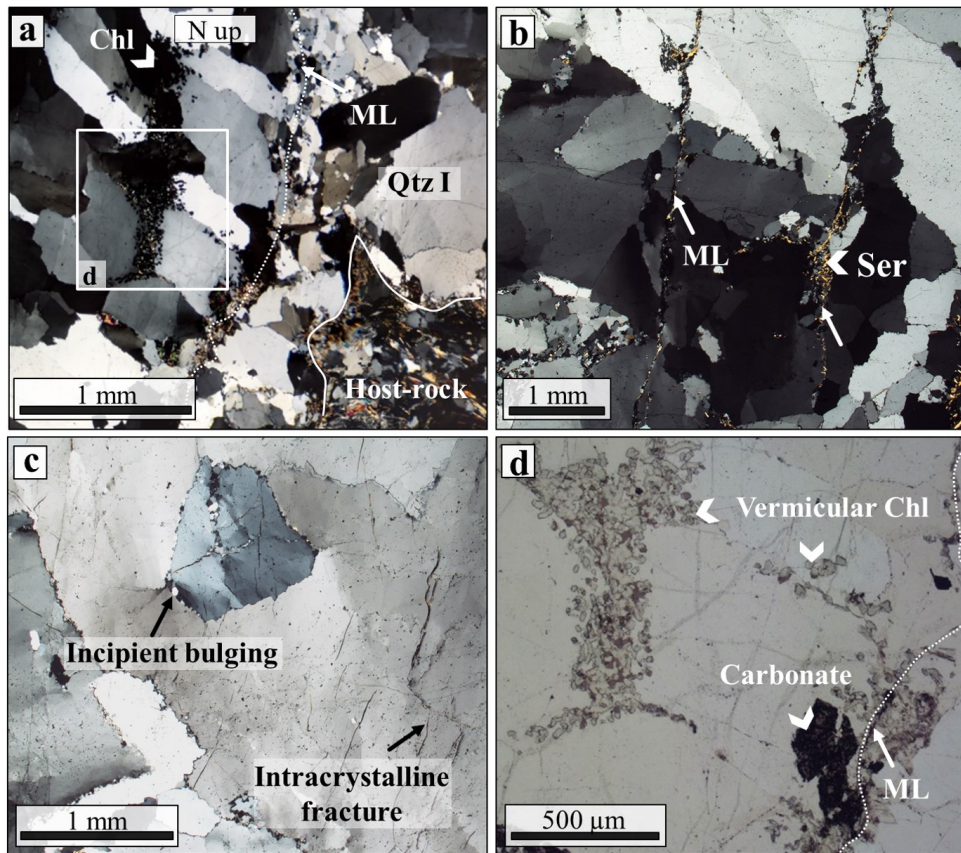
968
969 Figure 5. Microtextural characteristics of Qtz I from the damage zone of BFZ300 (samples PH21 and TPH-120 2). (a) Stitched microphotographs
970 of a Qtz I vein showing elongate-blocky texture with crystals growing obliquely with respect to the vein boundaries, which suggests growth
971 under oblique dilatation. A series of median lines (ML) are marked by (b) sericite crystals suggesting repeated crack-and-seal. Quartz crystals
972 show low temperature crystal-plastic deformation by undulose extinction and extinction bands. (c) Detail of plastic deformation in damage zone
973 quartz veins: distorted crystals showing incipient bulging and intracrystalline fracturing. (d) Detail (plane polarized light) of a ML and secondary
974 fractures both decorated by vermicular chlorite and aggregates of REE-bearing carbonate.
975
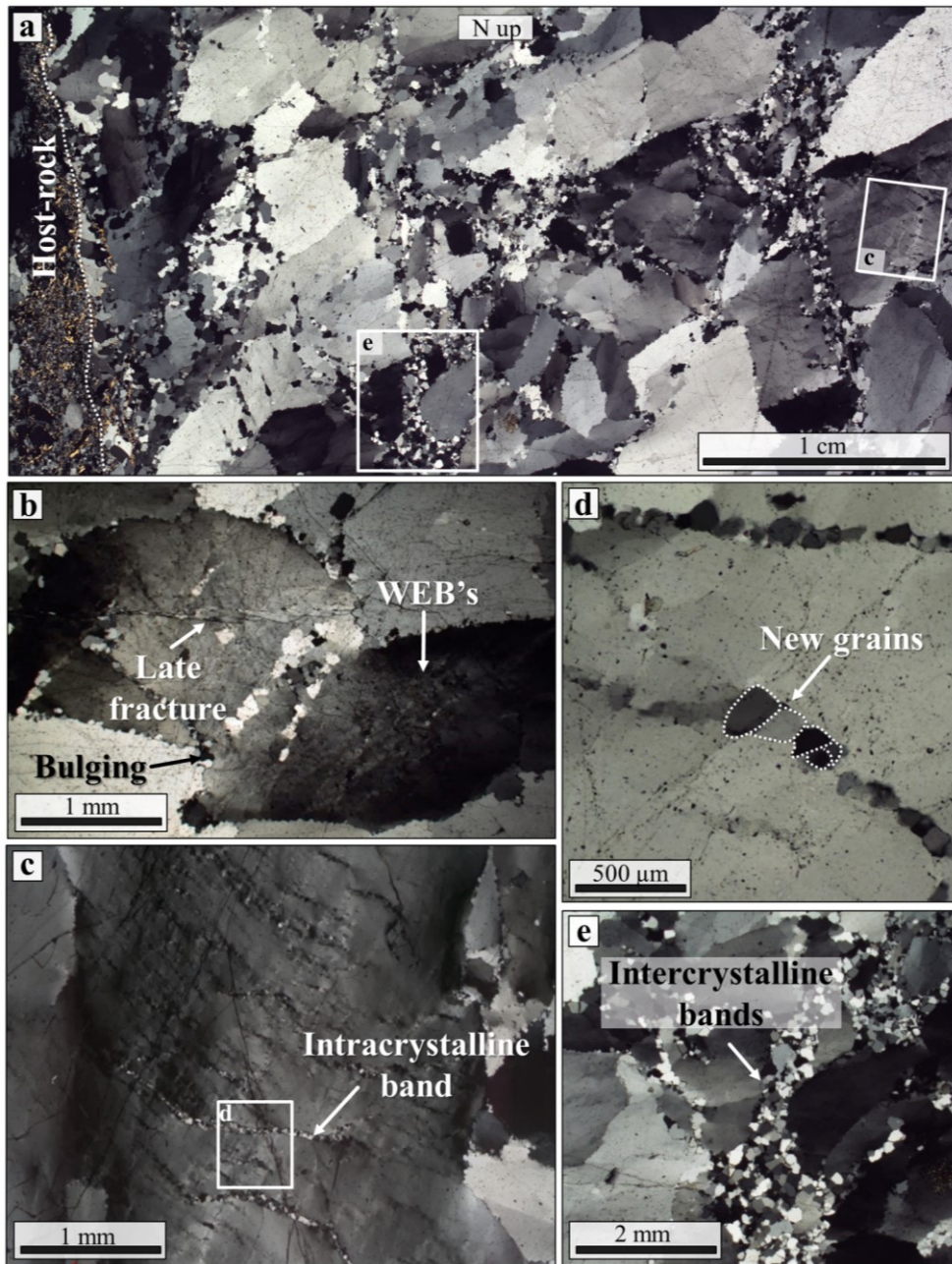
976
977 Figure 6. Microtextural characteristics of Qtz I from the BFZ300 core (sample TPH-120-4). (a) Stitched photomicrographs showing the typical
978 heterogeneous grain size of Qtz I (30-800 μm). (b) Evidence of plastic deformation of Qtz I from the fault core given by bulging of the largest
979 crystals, wide extinction bands and undulose extinction. Note the late brittle fractures crosscutting all the previously formed plastic features. (c)
980 Intracrystalline deformation bands within a large crystal. (d) Detail of (c) showing the typical grain size of the band (50-250 μm). Intracrystalline
981 deformation bands are oriented at <30° with respect to the BFZ300 vein walls and can be up to 2 mm in length. (e) Intercrystalline deformation
982 band showing a thickening at the triple junction of larger grains. These intercrystalline bands are parallel to the strike of BFZ300.
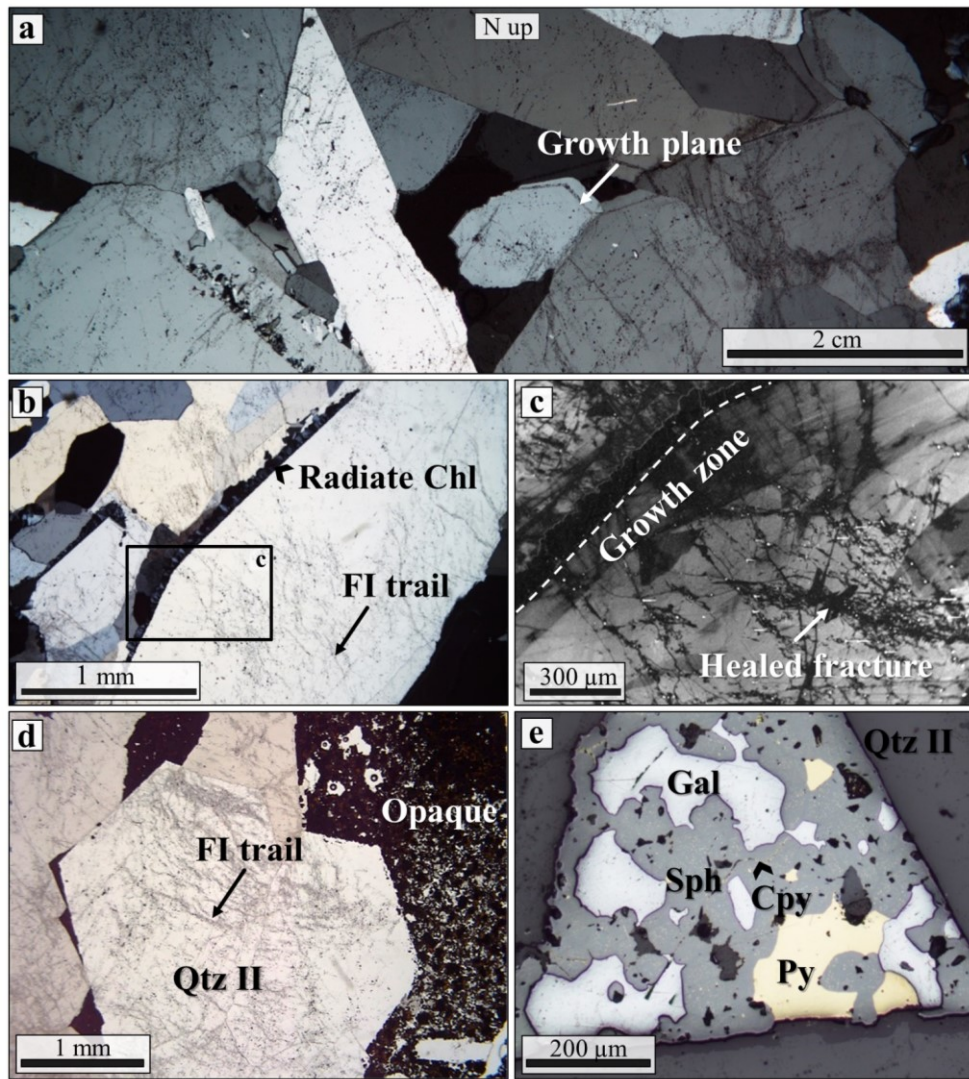
983
Figure 7. Microstructural characteristics of Qtz II from BFZ300 (samples TPH-120-6, PH22). (a) Stitched photomicrographs of Qtz II vein from
the fault core. Notice the coarse quartz crystals and their elongated-blocky texture. Primary growth textures are sometimes visible and are marked
by solid inclusions and decrepitated FIAs. (b) Radiate chlorite crystals along a prismatic Qtz II crystal boundary. Note that Qtz II is crosscut by
numerous trails of FIs. (c) Panchromatic cathodoluminescence image of the same large Qtz II crystal from panel b, showing radiate chlorite
along the crystal boundary and a primary growth zone cut by a set of healed fractures. (d) Euhedral quartz crystals set within opaque phases and
crosscut by a network of thin microfractures. (e) Reflected light photomicrograph showing the opaque mineral assemblage typically associated
with Qtz II, i.e. subhedral to anhedral sphalerite, pyrite, and galena. Chalcopyrite is a minor phase and occurs as small round inclusions within
sphalerite (chalcopyrite "disease") or as large subhedral/anhedral masses together with galena.

992
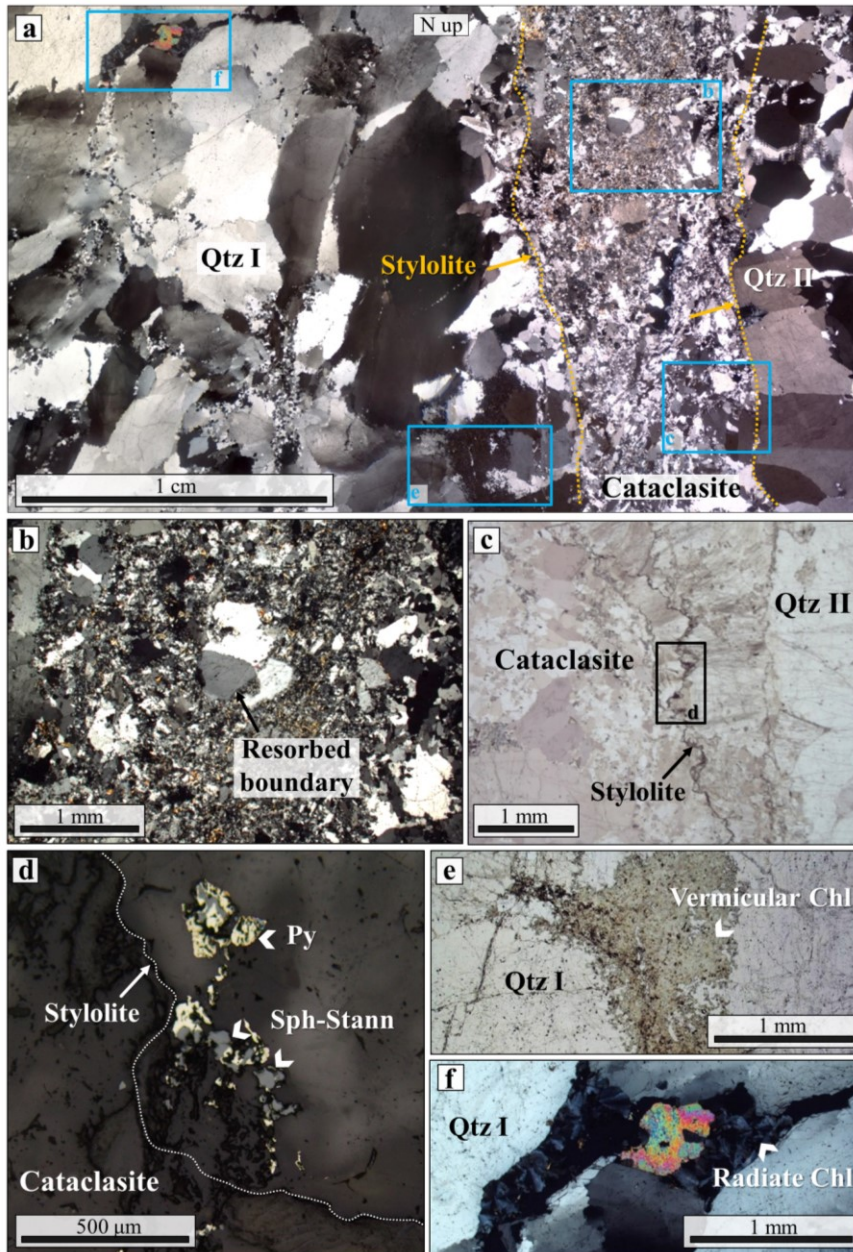
Figure 8. Microstructures of the cataclasite juxtaposing Qtz I and Qtz II veins (sample TPH-120-4). (a) Stitched photomicrographs covering the contact between the two quartz veins and the intervening 5 mm-thick cataclastic band. (b) Cataclastic band containing large Qtz I fragments (8-12 mm) embedded within a finer matrix (20-200 μm in size) of sericite and recrystallized quartz. The largest crystals show lobate boundaries, suggesting dissolution and local resorption along the clast-matrix interface. (c) Stylolite seams at the boundary of the cataclasite that strike parallel to the BFZ300. (d) Reflected-light photomicrograph showing anhedral to subhedral pyrite, chalcopyrite, stannite, and sphalerite arranged along the stylolite as residual products of pressure solution. (e) Vermicular and radiate (f) chlorite aggregates associated with Qtz I close to the cataclastic band.
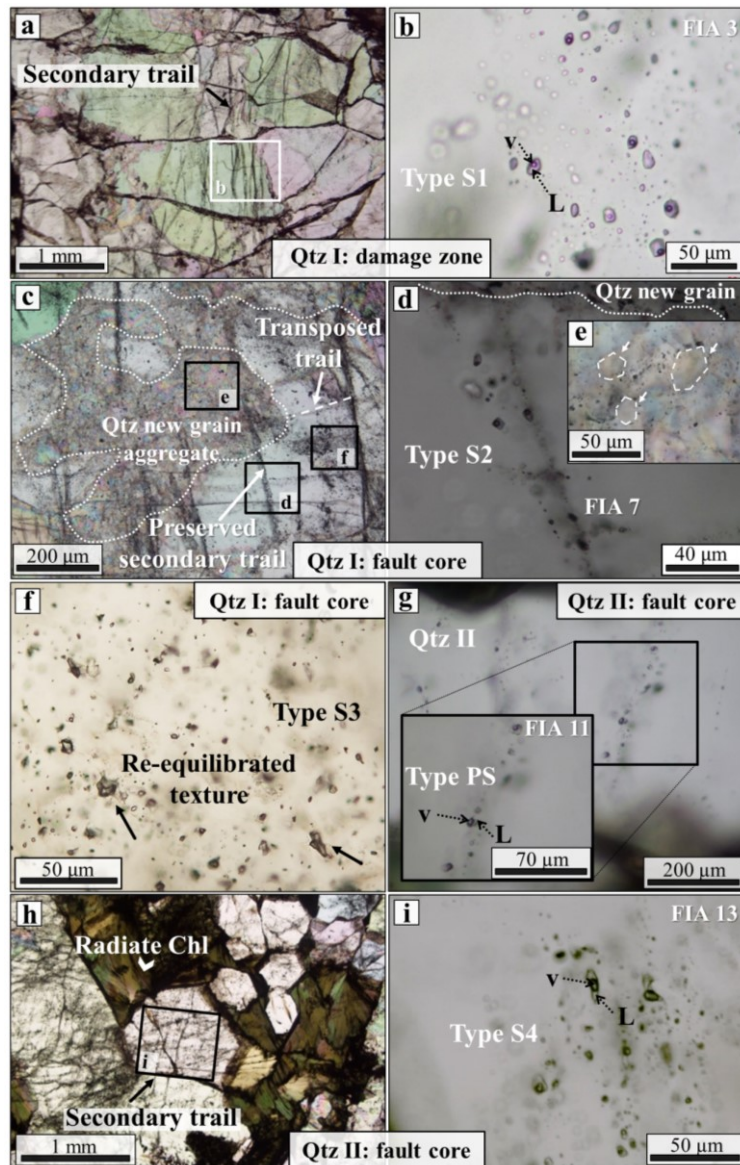
Figure 9. Characteristics textures of FIAs hosted within the BFZ300 quartz (samples PH21, TPH-120-4, TPH-120-6). (a) Secondary trails crosscutting large Qtz I crystals of the damage zone. (b) Detail of (a) showing the phase ratios of one of the studied secondary assemblages (FIA3), most representative of Type S1 FIA. (c) Long secondary transgranular trails crosscutting Qtz I of the fault core, dismembered by intercrystalline fractures, infilled by quartz new grains. Qtz I fault core also hosts set of short sub-trails developed at high angle with respect to the long trails. (d) Detail of Type S2 FIA entrapped along a preserved secondary fracture trail. (e) Small inclusions (<1μm) arranged along the boundaries of new polygonal quartz. (f) Example of Type S3 FIA arranged as isolated clusters inside ductile deformed fault core Qtz I. These trails formed during a brittle deformation stage that pre-dates ductile re-crystallization. (g) Pseudosecondary FIA associated with Qtz II-chlorite (FIA11). The enlargement shows the phase ratio details. (h) Small scale view of secondary FIAs crosscutting Qtz II. (i) Detail of secondary trails crosscutting euhedral Qtz II (FIA 13). In all photographs north points up.
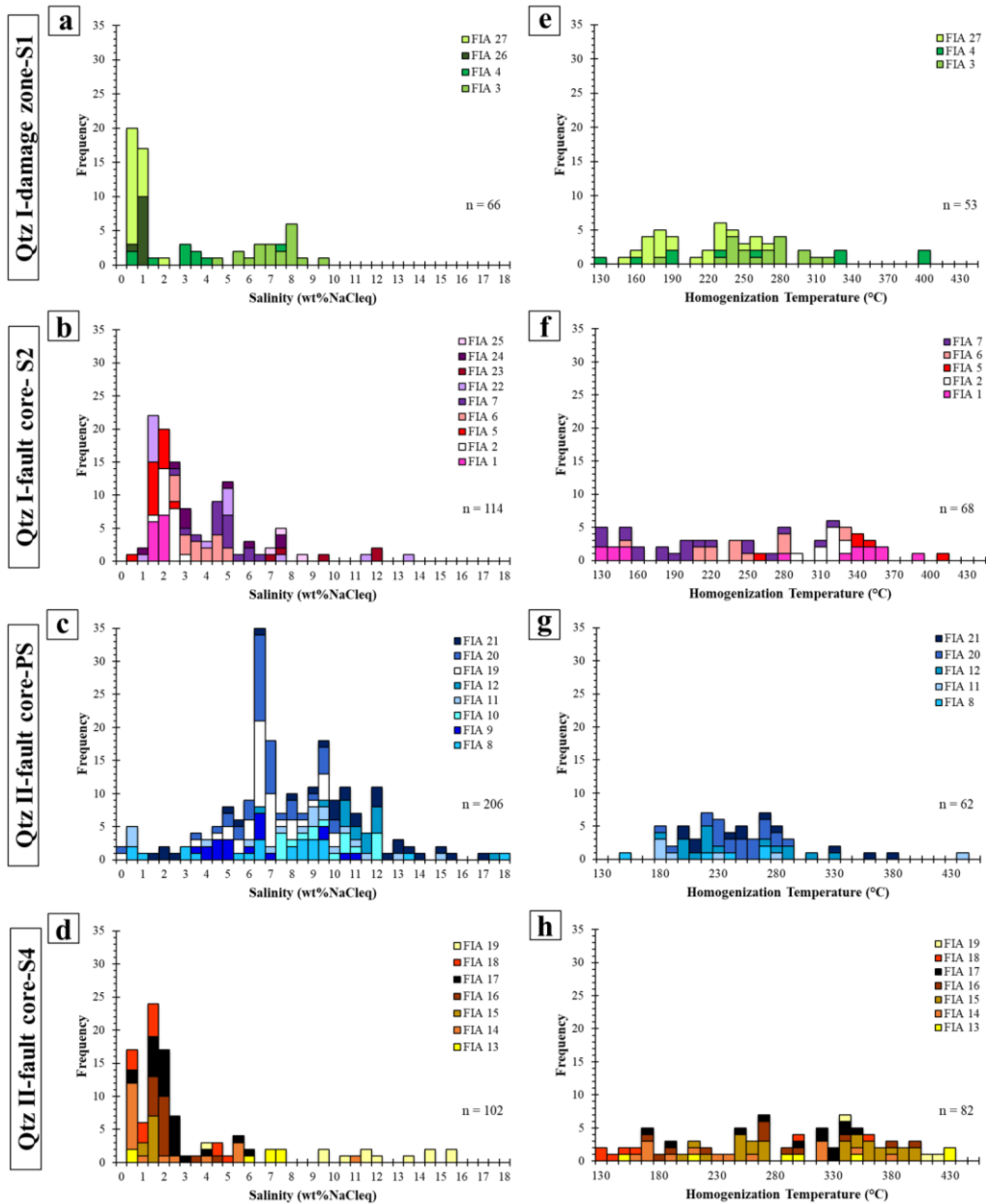
Figure 10. Microthermometric data of the studied FIAs. Panels a-d show the bulk salinities of individual FIAs calculated from the Tmice data, while panels e-h refer to the temperatures of final homogenization of the same assemblages. Notice that the data report the properties of individual FIAs according to their occurrence within Qtz I of the damage zone, Qtz I from the fault core, and Qtz II from the fault core. Notice that pseudosecondary (PS) and secondary (S) FIAs identify progressive later stages of fluid entrapment, and can be used to constrain the fluid properties in the fault zone. Notice also that the measured ranges of Th_{tot} spread across T intervals that are too large to represent entrapment at equilibrium (e.g., FIA7 of Qtz I from fault core: 130-320 °C), which suggests post-entrapment re-equilibration of the inclusions. Fluid bulk composition is expressed as salinity, which is conventionally reported as weight percent of NaCl equivalents (wt%NaCleq, Roedder,1984).
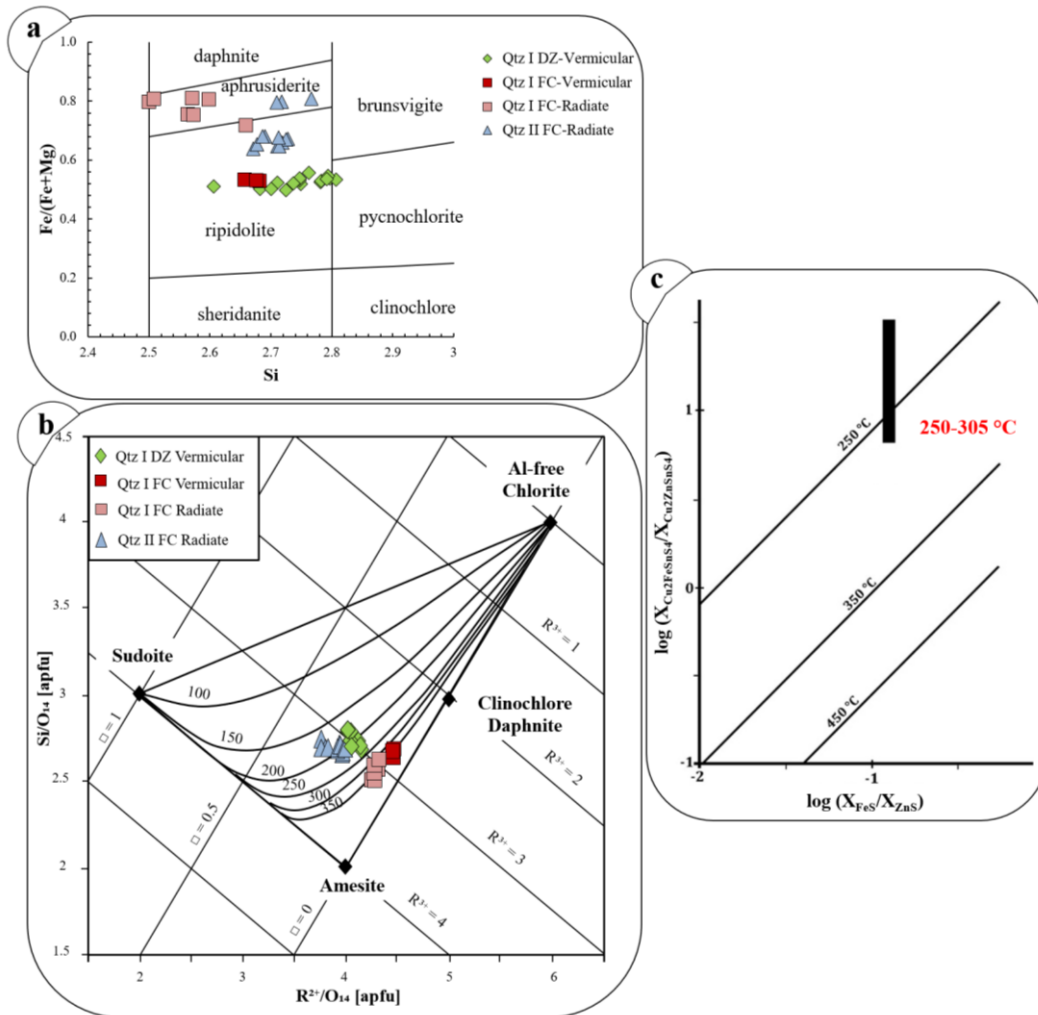
1020
1021 Figure 11. Chlorite chemical composition diagram and mineral-pair geothermometry applied to the assemblages of the Qtz I- and Qtz II veins.
1022 (a) Chlorite compositional diagram based on Hey (1954). Green, red, pink and light blue symbols indicate distinct chlorite textures in association
1023 with Qtz I and Qtz II veins. (b) Chlorite-quartz formation temperature estimated using the method of Bourdelle and Cathelineau (2015). The
1024 maximum temperature is from the Qtz I-chlorite pair from the fault core. (c) Estimated temperature of formation of sphalerite-stannite in
1025 association with Qtz II vein (based on Shimizu & Shikazono (1985). The region of the plot that was calibrated with this geothermometer lies
1026 between the 250 and 450 °C isotherms.
1027
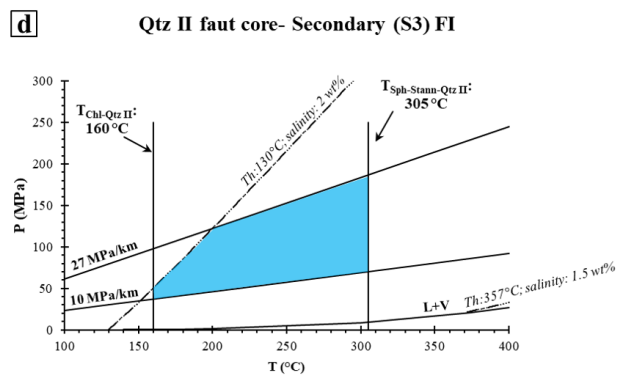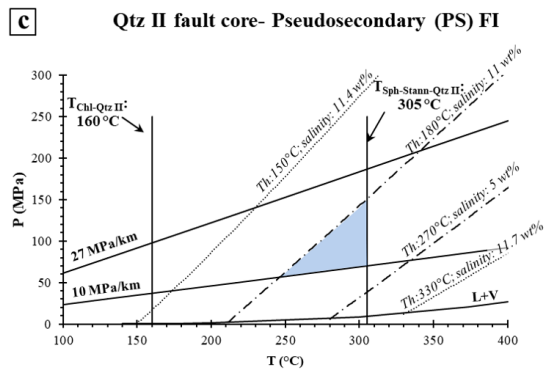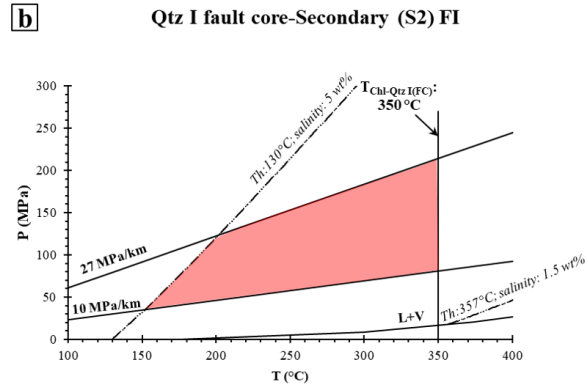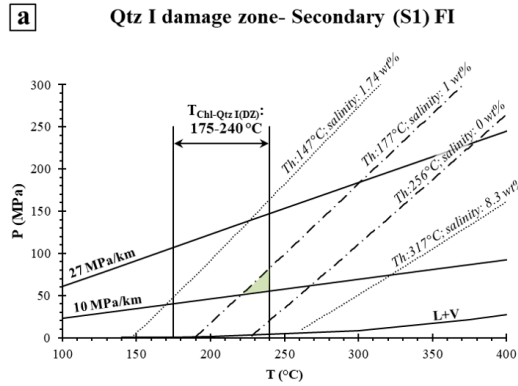
1028
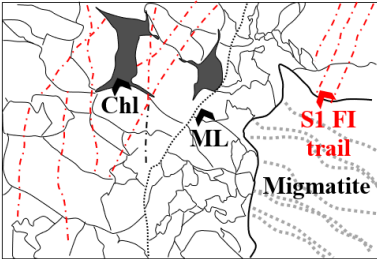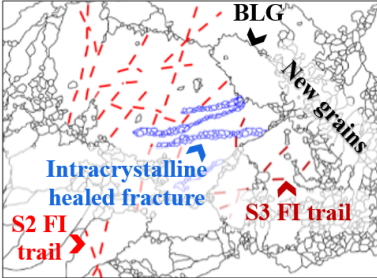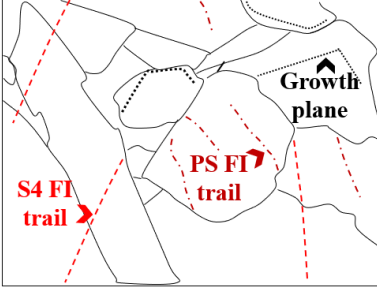
1029   Figure 12. P-T diagrams showing the ranges of PT trapping conditions of the analysed fluid inclusions: (a) secondary inclusions in Qtz I from
1030 the fault damage zone; (b) secondary inclusions from Qtz I in the fault core; (c) pseudosecondary inclusions trapped in Qtz II in the fault core
1031 and (d) secondary inclusions in the Qtz II. Thin dashed lines indicate maximum and minimum isochores of FIAs in each structural domain. The
1032 coloured areas identify the probable PT trapping ranges defined by: i) the slope and position of the fluid inclusion isochores as determined by
1033 the most representative salinity and homogenization temperature range (Supplementary Material for details); ii) mineral pairs geothermometry
1034 and iii) hydrostatic and lithostatic fluid pressures computed assuming a regional geothermal gradient of c. 40 °C/km (assuming retrograde
1035 conditions of 4 kbar and 650 °C, from Kärki and Paulamäki, 2006). The liquid-vapour equilibrium curve for the H_2O-NaCl modeled fluid is also
1036 indicated.

1037

1038
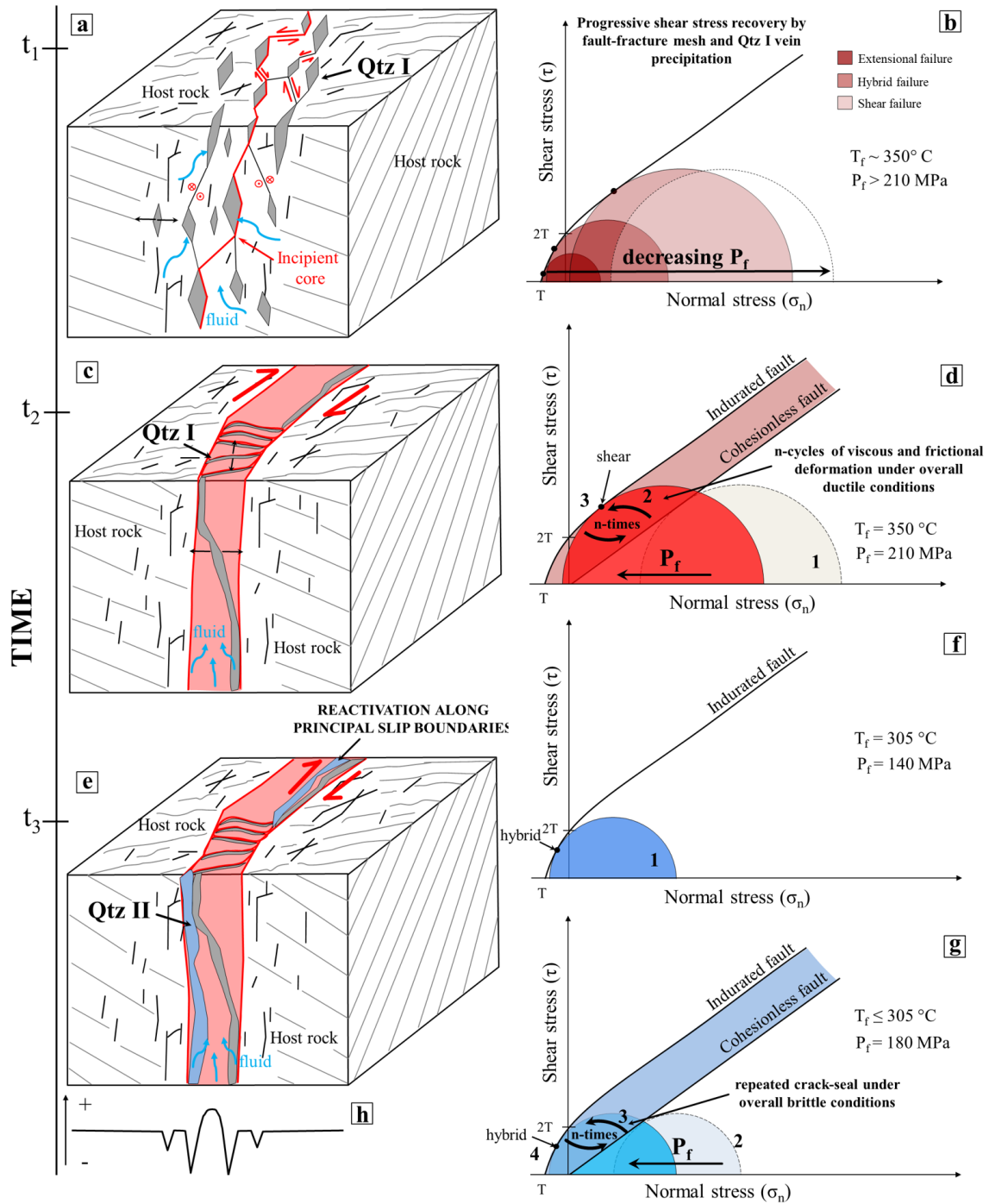
Figure 13. Conceptual model of the temporal and mechanical evolution of the BFZ300 fault zone (see text for more details). Grey lines: traces of metamorphic foliation. Black lines: fractures related to the BFZ300 structural development. (a) Initial embrittlement of the migmatitic basement occurred by fracture coalescence (red line) under (b) initial lower differential stress conditions and high fluid pressure and followed by a transient increase of differential stress. A first generation of quartz veins (Qtz I) precipitated inside the diffuse network of joints and hydrid/shear fractures which formed during this first deformation stage. (c) Progressive strain localization and fluid channeling within the fault core occurred by (d) episodically renewed fluid-pressure build-up driven by cycles of brittle and ductile deformation. (e-g) Progressive exhumation and cooling of the fault system occurred concomitant with several brittle reactivation episodes of the fault zone under hybrid conditions and fluid pressure lower than during the previous deformational stages. Lastly, a second generation of quartz veins (Qtz II) was emplaced, mainly along the principal slip boundaries of the fault core, following the Qtz I vein as shown by (h) the strenght profile across the fault architecture, that suggests lower tensile strength values (and hence higher reactivation potential) along the Qtz I vein / host rock walls.

1049 Table 1: Schematic summary of main microstructures, fluid properties, and PT deformation conditions in the quartz veins of the BFZ300 fault.

Structural zone and sample	Qtz type	Deformation type	Microstructures	Microthermometric properties	Fluid pressure (P_f) and mineral pair thermometry
Damage zone (PH-21)	Qtz I	Brittle/Ductile		T_{mice} S1: -0.1 to -5.9 °C T_{htot} S1: 150-400 °C	$T_{Chl-QtzI\ (DZ)}$: 175-240 °C P_f (S1): 50-80 MPa
Fault core (TPH120-4A)	Qtz I	Cyclic Brittle/Ductile		T_{mice} S2: -0.4 to -8.2 °C T_{htot} S2: 130-410 °C	$T_{Chl-QtzI\ (FC)}$: 350 °C P_f (S2) 30-210 MPa
Fault core (TPH120-6) (TPH120-4)	Qtz II	Brittle		T_{mice} PS: -0.1 to -13.6 °C T_{htot} PS: 150-440 °C T_{mice} S4: 0 to -11 °C T_{htot} S4: 130-430 °C	$T_{Chl-QtzII}$: 160-220 °C $T_{Sph-Stann-Qtz\ II}$: 250-305 °C P_f(PS): 50-140 MPa P_f(S4): 40-180 MPa

1050
1051 Note: microstructures are coupled with the corresponding FI types and PT constraints derived from the collected dataset. See text for more explanations.
1052 Notice that we combine structural and geochemical data to constrain the relationships between stages of mineral-scale deformation and fluid circulation,
1053 which in turn defines the relative chronology of stages of fluid flow during faulting.
1054 ML: median line; Blg: bulging.
1055
1056
1057

1058

1059

1060

Table 2: Chlorite EPMA from various structural zones of BFZ300

Sample	4A	4A	4A	4A	4A	4A	PH21	PH21	PH21	2	2	2	6	6	6	6
Structural zone	FC	FC	FC	FC	FC	FC	DZ	DZ	DZ	DZ	DZ	DZ	FC	FC	FC	FC
Quartz type	Qtz I	Qtz I	Qtz I	Qtz I	Qtz I	Qtz I	Qtz I	Qtz I	Qtz I	Qtz I	Qtz I	Qtz I	Qtz II	Qtz II	Qtz II	Qtz II
Textural type	Verm	Verm	Verm	Rad	Rad	Rad	Verm	Verm	Verm	Verm	Verm	Verm	Rad	Rad	Rad	Rad
Na_2O	0.04	0.07	0.00	0.08	0.08	0.03	0.05	0.02	0.04	0.03	0.01	0.05	0.04	0.06	0.01	0.01
TiO_2	0.02	0.01	0.00	0.00	0.03	0.01	0.09	0.04	0.01	0.01	0.01	0.03	0.03	0.03	0.04	0.13
MnO	0.59	0.65	0.62	0.53	0.56	0.48	0.24	0.24	0.30	0.48	0.37	0.43	0.64	0.57	0.71	0.60
K_2O	0.06	0.02	0.04	0.07	0.06	0.04	0.01	0.01	0.03	0.10	0.05	0.07	0.03	0.02	0.05	0.01
MgO	13.66	13.79	13.74	6.61	5.13	6.75	13.95	14.06	13.29	12.85	12.57	12.59	4.85	4.87	8.73	8.05
SiO_2	25.49	26.00	25.83	23.62	22.89	23.91	27.24	27.02	27.49	27.43	27.88	27.79	25.63	25.64	26.5	26.13
Cr_2O_3	0.00	0.01	0.04	0.00	0.00	0.06	0.04	0.03	0.06	0	0.06	0.01	0	0.02	0.01	0
FeO	27.86	27.74	27.87	36.61	38.49	36.75	24.68	25.21	26.07	25.97	26.06	25.77	34.26	33.84	30.08	30.47
CaO	0.03	0.04	0.05	0.00	0.06	0.03	0.01	0.02	0	0.05	0.05	0.03	0.01	0.04	0.04	0.02
Al_2O_3	22.04	22.13	22.00	22.89	23.35	22.98	24.13	24.75	24.91	24.02	23.48	23.21	24.23	24.64	24.49	25.02
Cl	0.00	0.00	0.01	0.03	0.02	0.04	0.01	0	0	0.01	0	0	0.03	0.02	0.02	0.01
Total	89.78	90.45	90.20	90.44	90.67	91.09	90.69	91.42	92.23	91.12	90.81	90.08	89.82	89.94	90.78	90.48
No. ions in formula Based on 28 (O,OH)																
Na	0.02	0.03	0	0.03	0.03	0.01	0.02	0.01	0.01	0.01	0.01	0.02	0.02	0.03	0	0.01
Ti	0	0	0	0	0	0	0.01	0.01	0	0	0.01	0	0.01	0.0	0.01	0.02
Mn	0.10	0.11	0.11	0.10	0.10	0.09	0.04	0.04	0.05	0.08	0.06	0.07	0.12	0.10	0.12	0.11
K	0.01	0	0.01	0.02	0.02	0.01	0	0	0.01	0.02	0.01	0.02	0.01	0	0.01	0
Mg	4.25	4.25	4.25	2.14	1.68	2.17	4.18	4.19	3.93	3.86	3.79	3.82	1.55	1.55	2.69	2.49
Si	5.32	5.37	5.36	5.14	5.02	5.15	5.48	5.40	5.46	5.53	5.64	5.66	5.49	5.47	5.48	5.43
Cr	0	0	0.01	0	0	0.01	0.01	0	0.01	0	0.01	0	0	0	0	0
Fe^{2+}	4.86	4.79	4.83	6.66	7.06	6.62	4.15	4.21	4.33	4.38	4.40	4.39	6.14	6.04	5.20	5.29
Ca	0.01	0.01	0.01	0	0.01	0.01	0	0	0	0.01	0.01	0.01	0	0.01	0.01	0
Al	5.42	5.39	5.38	5.86	6.04	5.84	5.72	5.83	5.83	5.71	5.59	5.57	6.12	6.20	5.97	6.13
Cl	0	0	0.01	0.01	0.01	0.01	0	0	0	0	0	0	0.01	0.01	0.01	0
Fe	4.86	4.79	4.83	6.66	7.06	6.62	4.15	4.21	4.33	4.38	4.40	4.39	6.14	6.04	5.20	5.29
Al Tetr	2.68	2.63	2.64	2.86	2.98	2.85	2.52	2.60	2.54	2.47	2.37	2.34	2.51	2.53	2.52	2.57
Al Oct	2.73	2.76	2.73	3.00	3.06	2.99	3.20	3.22	3.29	3.24	3.23	3.23	3.61	3.67	3.45	3.56
Fe/(Fe+Mg)	0.53	0.53	0.53	0.76	0.81	0.75	0.50	0.50	0.52	0.53	0.54	0.53	0.80	0.79	0.66	0.68
Based on 28 (O,OH)																
R^{2+}	9.11	9.04	9.08	8.80	8.74	8.79	8.33	8.40	8.26	8.24	8.19	8.21	7.69	7.59	7.90	7.79
Si	5.32	5.37	5.36	5.14	5.02	5.15	5.48	5.40	5.46	5.53	5.64	5.66	5.49	5.47	5.48	5.43
Based on 14 (O,OH)																
R^{2+}	4.55	4.52	4.54	4.40	4.37	4.40	4.17	4.20	4.13	4.12	4.10	4.10	3.84	3.79	3.95	3.89
Si	2.66	2.68	2.68	2.57	2.51	2.58	2.74	2.70	2.73	2.77	2.82	2.83	2.75	2.74	2.74	2.71

1071

1072   Table 3: Representative EPMA of sulphides associated with Qtz II

Analysis	Structural zone	Qtz type	Mineral	S	Fe	Cu	As	Pb	Ni	Zn	Ti	Sn	Total
TPH120-6-14	Core	II	pyrite	55.02	47.50	0.01	0.00	0.00	0.02	0.00	0.00		102.55
TPH120-6-17	Core	II	pyrite	54.08	47.19	0.00	0.01	0.00	0.00	0.00	0.00		101.28
TPH120-6-18	Core	II	sphalerite	34.46	6.46	0.09	0.01	0.00	0.03	59.62	0.02		100.69
TPH120-6-19	Core	II	sphalerite	34.48	6.24	0.08	0.06	0.00	0.04	59.61	0.02		100.53
TPH120-4A-34	Core	II	pyrite	54.49	47.40	0.05	0.00	0.00	0.00	0.00	0.00		101.94
TPH120-4A-35	Core	II	pyrite	54.13	47.26	0.02	0.04	0.00	0.00	0.01	0.55		102.01
TPH120-4A-38	Core	II	galena	13.40	0.00	0.00	0.00	86.63	0.00	0.32	0.01		100.36
TPH120-4A-59	Core	II	galena	13.50	0.06	0.00	0.01	87.04	0.00	0.10	0.01		100.72
TPH120-4A-40	Core*	II	sphalerite	35.06	9.46	0.05	0.00	0.00	0.00	56.74	0.01		101.32
TPH120-4A-43	Core*	II	sphalerite	34.69	9.04	0.01	0.03	0.00	0.00	57.51	0.01		101.28
TPH120-4A-41	Core	II	chalcopyrite	35.40	30.53	33.51	0.00	0.00	0.00	1.32	0.00		100.76
TPH120-4A-42	Core	II	chalcopyrite	35.78	30.78	33.59	0.03	0.00	0.01	1.22	0.01		101.42
TPH120-4A-19	Core **	II	stannite	29.79	12.53	28.41	0.07	0.08	0.00	0.92	0.000	27.86	99.66
TPH120-4A-22	Core **	II	sphalerite	33.82	8.15	0.06	0.00	0.03	0.02	57.27	0.006	0.00	99.36

1073   Note: * - located within cataclastic band and close to stylolite. ** - located along stylolite
1074   Sphalerite and stannite compositions from locations indicated by ** have been used to calculate the temperatures of sphalerite-stannite equilibrium following the
1075   geothermometer of Shimizu and Shikazono (1985). See text for more explanations.

1076

1077
1078